Computers and Structures 280 (2023) 106987

Contents lists available at ScienceDirect

Computers and Structures

journal homepage: www.elsevier.com/locate/compstruc

Simple modeling of reinforced masonry arches for associated and non-associated heterogeneous limit analysis

Yiwei Hua, Gabriele Milani *

Department of Architecture, Built Environment and Construction Engineering, Politecnico di Milano, Piazza Leonardo da Vinci 32, 20133 Milan, Italy

ARTICLE INFO

Article history:
Received 8 September 2022
Accepted 25 January 2023

Keywords:
Heterogeneous limit analysis
Reinforcement
Masonry arch
Associated flow
Non-associated flow

ABSTRACT

This paper proposes a limit analysis heterogeneous model for masonry arches in presence of innovative strengthening, rigid blocks, and joints reduced to interfaces. The reinforcement is considered in a simplified but effective way in the context of limit analysis, suitably modifying the admissibility conditions of the constitutive law that governs the behavior of contact joints. First, the force resultants at the interface after the reinforcement is investigated. Based on that, the yield condition and flow rule in the standard heterogeneous limit analysis formulation are updated. This approach is applied to solve both associated and non-associated sliding cases. For benchmarking purposes, the collapse of a 2D arch with both-side Fiber Reinforced Polymer (FRP) reinforcement is analyzed, followed by several parametric studies and a cost-benefit study. Collapse analysis of a real arch tested in-situ is also presented for further verification. The results show that in some cases an incorrect collapse mechanism and an overestimated ultimate load would be obtained through associated limit analysis. Such overestimation may become very significant once the reinforcement is taken into account. The presented cases illustrate that the maximum overestimation of the load could reach in meaningful cases of technical interest 91% of the associated prediction. This suggests the use of a non-associated flow rule to accurately predict the collapse load increase of reinforced arches. According to the cost-benefit study, it is recommended to strengthen at least half of the joints to guarantee an acceptable effect of the strengthening. The simulation of the collapse of the in-situ tested arch further proves the reliability of the proposed approach.

1. Introduction

Historical arch and vault masonry structures are widely diffused in the western and eastern worlds. Those peculiar constructions have been standing for a long era and many of them have become precious historical and monumental constructions that deserve to be preserved. Collapse analysis of these historical buildings has raised great concern in recent numerical studies. Commercial incremental-iterative-analysis packages, such as Finite element method [1] or Discrete element method [2–3], are usually time-consuming and probably meet convergence problems when analyzing the failure of the masonry. Thanks to the boom of Computational Operational Research, many optimization-based approaches were developed [4–5], where the collapse problem is formalized into an optimization problem and can be solved fast in a single step. Among these tools, heterogeneous limit analysis is becoming one of the standard tools for collapse analysis of those historical structures [6–10]. This powerful approach can not only precisely take into account the discrete nature of the masonry structures but quickly provide their collapse mechanism and ultimate load. As concluded in pioneering works [11–12], if an associated flow rule is employed, i.e., the vector of possible discontinuous velocities keeps orthogonal to the limit surface (Fig. 1a), the problem can be solved through robust linear programming (LP) software available in a single step. Unfortunately, as Drucker claimed [13], such associativity does not hold in most cases for a masonry structure, since it results in an unrealistic separation among the bricks when sliding takes place. A more reasonable choice for simulating the sliding is to use a classic Coulomb sliding friction law [14], which should be, however, non-associated (Fig. 1b). This complex problem has been tackled by many researchers in the last two decades (see for instance [15–18]). Two common strategies to find the solution of a non-associated limit analysis problem are linear complementary programming (LCP) [16] or sequential linear programming (SLP) [17]. The second approach, more recent, has the advantage that still uses linear programming to solve a complementarity problem within a certain iterative searching scheme, securing robustness

* Corresponding author.
E-mail addresses: yiwei.hua@polimi.it (Y. Hua), gabriele.milani@polimi.it (G. Milani).

https://doi.org/10.1016/j.compstruc.2023.106987
0045-7949/

Nomenclature

LIST OF SYMBOLS

ε	Normal discontinuous velocity at interface
γ	Sliding discontinuous velocity at interface
θ	Rotational discontinuous velocity at interface
n	Axial force at interface
s	Shear force at interface
$\bar{n}$	Normal resultant at interface
$\bar{s}$	Shear resultant at interface
$\bar{m}$	Moment at interface
e	Eccentric at interface
t	Height of the joint
c_0	Initial cohesion given by mortar
φ	Sliding friction angle
η	Rotational friction angle
ψ	Sliding dilation angle
A	Area of the interface
ε_j	Normal discontinuous velocity at joint j
γ_j	Sliding discontinuous velocity at joint j
θ_j	Rotational discontinuous velocity at joint j
$\bar{n}_j$	Normal resultant at joint j
$\bar{s}_j$	Shear resultant at joint j
$\bar{m}_j$	Moment at joint j
φ_j	Sliding friction angle of joint j
η_j	Rotational friction angle of joint j
ψ_j	Sliding dilation angle of joint j
A_j	Area of joint j
$c_{0,j}$	Initial cohesion given by mortar at joint j
u_i	Horizontal centroid velocity at block i
v_i	Vertical centroid velocity at block i
ω_i	Rotational velocity at block i
W_i	Weight of block i
F^i_{Lx}	Live load acting at block i along $\times$ direction
F^i_{Ly}	Live load acting at block i along y direction
F^{in}_t	Intrados tensile force due to reinforcement
F^{ex}_t	Extrados tensile force due to reinforcement
F^{in}_s	Intrados sliding force due to reinforcement
F^{ex}_s	Extrados sliding force due to reinforcement
$F^{\text{in}}_{t,\max}$	Maximum intrados tensile cohesion
$F^{\text{ex}}_{t,\max}$	Maximum extrados tensile cohesion
$F^{\text{in}}_{s,\max}$	Maximum intrados sliding cohesion
$F^{\text{ex}}_{s,\max}$	Maximum extrados sliding cohesion
f_{bt}	Tensile strength of brick
f_{bc}	Compressive strength of brick
β	Peeling angle of FRP
l_{ed}	Optimal bond length of FRP
t_{f}	thickness of FRP
E_{f}	Young's Module of FRP
b_{f}	Strengthening depth
f_{bd}	Design bond strength of FRP
σ_{r}	Debonding strengthen of SRG
t_{eq}	Equivalent thickness of the SRG
α	Load multiplier
N_{re}	Number of the reinforced joint
$\mathbf{L}_{\text{re}}$	Matrix of strengthening scheme
$\mathbf{A}$	equilibrium matrix
$\mathbf{x}$	unknown joint resultant
$\mathbf{f}_D$	Vector of dead load
$\mathbf{f}_L$	Vector of live load
$\mathbf{N}$	constitutive constraint operator
$\mathbf{z}$	Slackness variable for failure surface
$\mathbf{c}_0$	Initial cohesion force given by mortar
$\mathbf{c}_m$	Spurious cohesion given by reinforcement
$\mathbf{q}$	unknown joint discontinuous velocities
$\mathbf{u}$	unknown centroid velocities at blocks
$\mathbf{p}$	resultant of the discontinuous velocities
$\mathbf{V}$	Transforming operator
$\mathbf{r}^i_j$	Vector from block i to joint j (centroid)
$\mathbf{e}^j_t$	Normal vector of joint j
$\mathbf{e}^j_n$	Tangential vector of joint j
$\mathbf{e}_x$	Unit vector of horizontal direction
$\mathbf{e}_y$	Unit vector of vertical direction

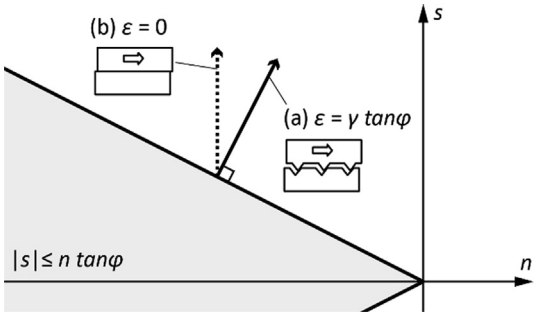

Fig. 1. Typical limit surface for normal force $\boldsymbol{n}$ and shear force $\boldsymbol{s}$ at joints, and different flow rules for discontinuous separation velocity ε and sliding velocity γ: (a) associative ("sawtooth") friction; (b) Coulomb (non-associated) friction.

even in case of large-scale problems. Note that the non-associated flow rule actually refers to the case where the dilation angle is not consistent with the friction angle. While in this paper, we would use this term to specify the zero-dilation case because it is more common for masonry structures.

On the other hand, owing to the development of composite materials, numerous innovative strengthening techniques have been employed to improve the structural performance of historical masonry buildings, the most diffused being probably the application of external FRP strips or FRCM grids. How to simulate such a strengthening effect through a standard heterogeneous limit analysis has gained growing attention, because limit analysis is much faster than a classic incremental elasto-plastic approach and is able to provide information that is extremely interesting in design, such as the ultimate load carrying capacity, the activating failure mechanism and, at least on critical sections, the stress distribution at collapse. Among current works, one of the critical drawbacks is that most of the approaches presented in the literature still employ the associated flow rule [19–23], which is not in line with the actual behavior of masonry, especially if reinforced. This is particularly true for arches, where the associativity may work only if a flexural failure mechanism characterized by the formation of four hinges triggers. As shown by Heyman, if the arch is not particularly squat, such hypothesis is very realistic in case of absence of reinforcement, but the presence of an external retrofitting tends to preclude the formation of a flexural hinge in those positions where the reinforcement is placed, giving raise to mixed failure mechanisms where sliding is also present. Furthermore, the reinforcement was mostly modeled by introducing extra elements [24–26]. Such modeling strategy is accurate but sometimes cumbersome especially when extended to 3D problems. To bridge these gaps, this paper

presents a simple modeling approach for masonry arches, including the strengthening effect within the frame of a simple heterogeneous limit analysis where blocks are assumed infinitely resistant, joints are reduced to interfaces with a cohesive-frictional behavior and no-extra elements are required for the reinforcement strips. The proposed approach is meant to be applied for both associated and non-associated formulations. Starting from the simple observation that the failure surface of the contact is found to change after strengthening [27–28], the major peculiarity of the procedure presented is the possibility to consider the reinforcement effect by merely modifying the constraint regarding the failure surface, without involving extra elements.

The organization of the paper is structured as follows: section 2 first investigates the change of the failure surface after strengthening. The formulation of the standard heterogeneous limit analysis, both associated and non-associated, is then updated considering such a strengthening effect. By implementing the aforementioned theory, section 3 analyzes the collapse of a benchmark 2D arch with both-side FRP reinforcement. The effect of the reinforcement is briefly summarized and the results of the collapse employing associated and non-associated flow rules are compared. Several parametric studies are carried out after that. After that, a cost-benefit study to find an optimal strengthening scheme is conducted in section 4. Finally, in section 5, we simulate the collapse of an arch experimentally tested in-situ, followed by detailed sensitivity analyses, as a verification. The acquired results are discussed and several critical conclusions are drawn in Section 6.

2. Methodology

To illustrate the change of the failure surface after the reinforcement, we first consider all the possible forces at a representative joint with both-side strengthening (Fig. 2). The reinforcement produces tensile forces (F_t^{ex} and F_t^{in}) when the joint separates (Fig. 2a), while once the sliding happens, F_s^{ex} and F_s^{in} are applied to the block because of the triggering of a peeling failure at the FRP-support interface (Fig. 2b). Taking these effects into account (Fig. 2c), the restriction of the forces at the interface can then be written as in Eq. (1) (a detailed deduction of this equation is given in Appendix A).

$$\begin{aligned}
&|e| = \left|\frac{\bar{m} - F_t^{\text{in}}\tan\eta + F_t^{\text{ex}}\tan\eta}{\bar{n} - F_t^{\text{in}} - F_t^{\text{ex}} - c_0 A}\right| \le \tan\eta \\
&\left(\bar{n} - F_t^{\text{in}} - F_t^{\text{ex}} - c_0 A\right)\tan\varphi + \left|\bar{s}\right| - F_s^{\text{in}} - F_s^{\text{ex}} \le 0 \\
&0 \le F_t^{\text{in}} \le F_{t,\max}^{\text{in}},\ 0 \le F_t^{\text{ex}} \le F_{t,\max}^{\text{ex}} \\
&0 \le F_s^{\text{in}} \le F_{s,\max}^{\text{in}},\ 0 \le F_s^{\text{ex}} \le F_{s,\max}^{\text{ex}}
\end{aligned} \tag{1}$$

where $(\bar{n}, \bar{s}, \bar{m})$ is the resultant vector at the interface (Fig. 2d); φ and η are the friction angle for rotation and sliding, respectively; $F_{t,\max}^{\text{in}}$, $F_{t,\max}^{\text{ex}}$, $F_{s,\max}^{\text{in}}$, and $F_{s,\max}^{\text{ex}}$ are the maximum forces that the reinforcement can provide at the interface; c_0 is the initial cohesion at the interface, usually provided by the mortar, and A represents the area of the contact. In the case of no-tension material, c_0 is zero.

The failure surfaces formed by those constraints are shown in Fig. 3. Compared with the original one [16], the region for the possible force state is enlarged due to the reinforcement. Specifically, $\bar{m}$–$\bar{n}$ surface is translated along the positive direction of $\bar{n}$ axis (Fig. 3a); $\bar{s}$–$\bar{n}$ surface, besides the transversely moving, is expanded along the $\bar{s}$ axis at the same time (Fig. 3b).

Constraints shown in Eq. (1) can be shaped into a matrix form, see the following Eq. (2) that is very similar to the yield condition used in a standard heterogeneous limit analysis [16]:

$$\mathbf{N}\mathbf{x} - \mathbf{c}_0 - \mathbf{c}_m = \mathbf{z},\ \ \mathbf{z} \le 0 \tag{2}$$

$\mathbf{c}_0$ is the vector collecting all the initial cohesion for each interface. Matrix $\mathbf{N}$ is named constitutive constraint operator, containing the friction angle of the contact for both sliding and rotation. For a specific contact j, the matrix $\mathbf{N}_j$ and vector $\mathbf{c}_{0,j}$ are given in Eq. (3), where the subscript j indicates the corresponding material parameter for the contact j.

$$\mathbf{N}_j = \begin{bmatrix} \sin\varphi_j & \cos\varphi_j & 0 \\ \sin\varphi_j & -\cos\varphi_j & 0 \\ \sin\eta_j & 0 & \cos\eta_j \\ \sin\eta_j & 0 & -\cos\eta_j \end{bmatrix},\ \mathbf{c}_{0,j} = \begin{bmatrix} c_{0,j}^{s+} \\ c_{0,j}^{s-} \\ c_{0,j}^{r+} \\ c_{0,j}^{r-} \end{bmatrix} = \begin{bmatrix} c_{0,j}A_j\sin\varphi_j \\ c_{0,j}A_j\sin\varphi_j \\ c_{0,j}A_j\sin\eta_j \\ c_{0,j}A_j\sin\eta_j \end{bmatrix} \tag{3}$$

It is worth mentioning that in Eq. (2) a spurious cohesion term $\mathbf{c}_m$ merely needs to be added to consider the effect of the strengthening. The components of $\mathbf{c}_m$ at a specific interface j are given in Eq. (4), which can be simply derived from the properties of the reinforced material:

$$\mathbf{c}_{m,j} = \begin{bmatrix} c_{m,j}^{s+} \\ c_{m,j}^{s-} \\ c_{m,j}^{r+} \\ c_{m,j}^{r-} \end{bmatrix} = \begin{bmatrix} \left(F_{t,\max}^{\text{in}} + F_{t,\max}^{\text{ex}}\right)\sin\varphi_j + \left(F_{s,\max}^{\text{in}} + F_{s,\max}^{\text{ex}}\right)\cos\varphi_j \\ \left(F_{t,\max}^{\text{in}} + F_{t,\max}^{\text{ex}}\right)\sin\varphi_j + \left(F_{s,\max}^{\text{in}} + F_{s,\max}^{\text{ex}}\right)\cos\varphi_j \\ 2F_{t,\max}^{\text{in}}\sin\eta_j \\ 2F_{t,\max}^{\text{ex}}\sin\eta_j \end{bmatrix} \tag{4}$$

The Lower Bound (LB) and Upper Bound (UB) associated formulations considering the effect of reinforcement can be then updated as illustrated hereafter in Eqs. (5) and (6), respectively:

$$\begin{aligned}
&\underset{\alpha,\mathbf{x},\mathbf{z}}{\text{maximize}} && \alpha \\
&\text{subject to} && \mathbf{A}\mathbf{x} = \alpha\mathbf{f}_{\text{L}} + \mathbf{f}_{\text{D}} \\
& && \mathbf{N}\mathbf{x} - \mathbf{c}_0 - \mathbf{c}_m = \mathbf{z} \\
& && \mathbf{z} \le 0
\end{aligned} \tag{5}$$

$$\begin{aligned}
&\underset{\mathbf{u},\mathbf{q},\mathbf{p}}{\text{minimize}} && -\mathbf{f}_D^T\mathbf{u} + \mathbf{c}_0^T\mathbf{p} + \mathbf{c}_m^T\mathbf{p} \\
&\text{subject to} && \mathbf{f}_L^T\mathbf{u} = 1 \\
& && \mathbf{A}^T\mathbf{u} = \mathbf{q} \\
& && \mathbf{N}^T\mathbf{p} = \mathbf{q},\ \ \mathbf{p} \ge 0
\end{aligned} \tag{6}$$

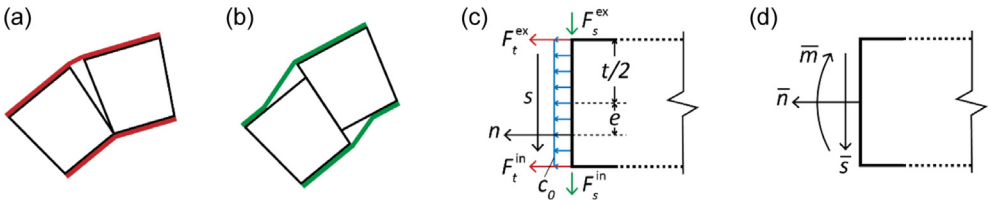

Fig. 2. Interface resultant forces after strengthening and equivalent description: (a) rotational failure; (b) sliding failure (c) possible joint forces when failure happens; (d) equivalent description.

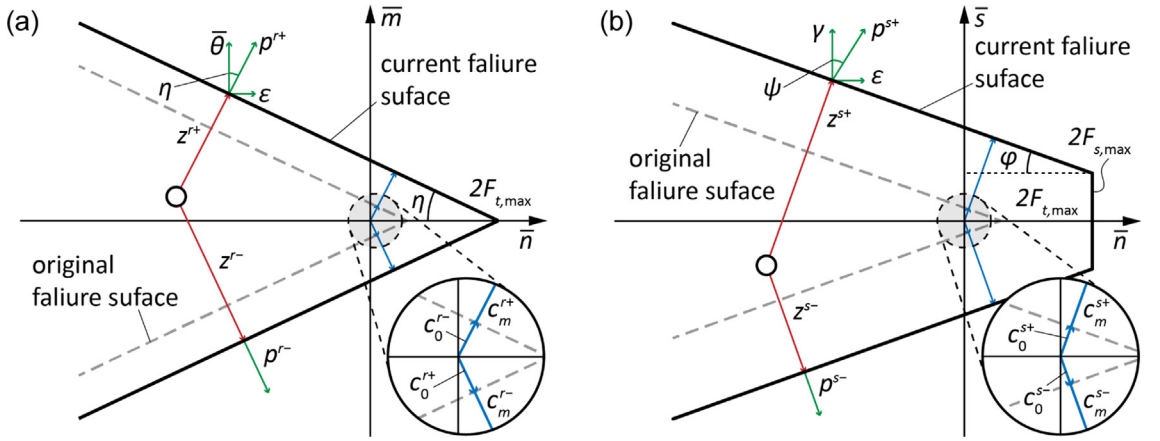

Fig. 3. Change of the failure surfaces due to the reinforcement: (a) $\bar{m}$–$\bar{n}$ limit surfaces; (b) $\bar{s}$–$\bar{n}$ limit surfaces.

Moreover, this technique is also applicable for the non-associated case, which can be easily incorporated within an existing SLP scheme [17]. In such SLP scheme, a non-associated problem is unpacked into a series of associated limit analyses. The friction angle is gradually reduced in each step, enforcing the limit surface to be horizontal in the Mohr plane (Fig. 4). The corresponding flow vector is adjusted simultaneously due to the associativity and the dilation angle will eventually vanish. As a consequence, these associated solutions will converge to a non-associated one.

Algorithm 1 (*SLP iterative procedure*).

1. Solve initial associated problems (5) and (6), get $\mathbf{x}_0$
2. Initial: $\xi_0 = 0.3$; $\xi_{\min} = 0.001$; $k = 0$; $tol = 10^{-6}$
3. **REPEAT**
4. Reduce ξ: $\xi_{[k+1]} \leftarrow \max\{\xi_{[k]}/2, \xi_{\min}\}$
5. Reduce frictional angle φ and update $\mathbf{N}_{[k+1]}$

$$\tan\varphi_{j,[k+1]} \leftarrow -\xi_{[k+1]}\left(\tan\varphi_j - \tan\psi_j\right) + \tan\psi_j \tag{7}$$

$$\mathbf{N}_{j,[k+1]} = \begin{bmatrix} \sin\varphi_{j,[k+1]} & \cos\varphi_{j,[k+1]} & 0 \\ \sin\varphi_{j,[k+1]} & -\cos\varphi_{j,[k+1]} & 0 \\ \sin\eta_j & 0 & \cos\eta_j \\ \sin\eta_j & 0 & -\cos\eta_j \end{bmatrix} \tag{8}$$

6. Update cohesion $\mathbf{c}_{[k+1]}$ by resultants $\mathbf{x}_{[k]}$ from previous step

$$\mathbf{c}_{[k+1]} \leftarrow -(1+\xi_{[k+1]})\cos\varphi_{[k+1]}\mathbf{V}\mathbf{x}_{[k]} + \mathbf{c}_0 \tag{9}$$

7. Solve new LB/UB problems and get $\mathbf{x}_{[k+1]}$

$$\begin{aligned} \underset{\alpha_{[k+1]},\mathbf{x}_{[k+1]},\mathbf{z}_{[k+1]}}{\text{maximize}} \quad & \alpha_{[k+1]} \\ \text{subject to} \quad & \mathbf{A}\mathbf{x}_{[k+1]} = \alpha_{[k+1]}\mathbf{f}_L + \mathbf{f}_D \\ & \mathbf{N}_{[k+1]}\mathbf{x}_{[k+1]} - \mathbf{c}_{[k+1]} - \mathbf{c}_m = \mathbf{z}_{[k+1]} \\ & \mathbf{z}_{[k+1]} \le 0 \end{aligned} \tag{10}$$

$$\begin{aligned} \underset{\mathbf{u}_{[k+1]},\mathbf{q}_{[k+1]},\mathbf{p}_{[k+1]}}{\text{minimize}} \quad & -\mathbf{f}_D^T\mathbf{u}_{[k+1]} + \mathbf{c}_{[k+1]}^T\mathbf{p}_{[k+1]} + \mathbf{c}_m^T\mathbf{p}_{[k+1]} \\ \text{subject to} \quad & \mathbf{f}_L^T\mathbf{u}_{[k+1]} = 1 \\ & \mathbf{A}^T\mathbf{u}_{[k+1]} = \mathbf{q}_{[k+1]} \\ & \mathbf{N}_{[k+1]}^T\mathbf{p}_{[k+1]} = \mathbf{q}_{[k+1]},\ \mathbf{p}_{[k+1]} \ge 0 \end{aligned} \tag{11}$$

8. Calculate error: $e = |\alpha_{[k+1]} - \alpha_{[k]}|/\alpha_{[k]}$
9. $k \leftarrow k + 1$
10. **UNTIL** $e < tol$

To consider the strengthening effect in non-associated problems, in a similar way it is possible to add such a cohesion $\mathbf{c}_m$ in the formulation of each iterative step. The updated SLP iterative scheme is listed in Algorithm 1 (see [17,29] for further information). Here in Eq. (9), matrix $\mathbf{V}$ is the operator transforming the associated sliding to the target non-associated sliding [29]. For

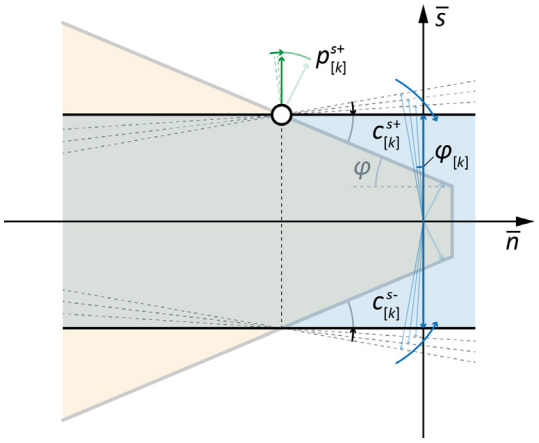

Fig. 4. Adjustment of the limit surfaces during the iterations (zero-dilation case).

contact j, $\mathbf{V}_j$ is given in Eq. (12), where ψ_j is the corresponding dilation angle, as noted in Fig. 3b. In the associated sliding case, i.e. $\varphi_j = \psi_j$, we have $\mathbf{V} = 0$ and the algorithm is degenerates into the associated formulation (5) and (6).

$$\mathbf{V}_j = \begin{bmatrix} \tan\varphi_j - \tan\psi_j & 0 & 0 \\ \tan\varphi_j - \tan\psi_j & 0 & 0 \\ 0 & 0 & 0 \\ 0 & 0 & 0 \end{bmatrix} \tag{12}$$

Note that this SLP iterative algorithm can also be applied to the case where a non-zero dilation angle is present, while in this paper, we remain in the zero-dilation case, assigning ψ_j as zero because it is the typical situation studied in masonry structure [10,14–18,29]. Similar to the associated flow, the non-zero dilation angle will give rise to obvious separation among the bricks and thus leading to more dissipation at the interface. Intuitively, the ultimate load for the collapse with non-zero dilation should be larger than that for zero dilation. Therefore, the presented results for zero-dilation collapse can, on the other hand, give a lower bound for these cases with non-zero dilation.

3. Results

3.1. Benchmark case study: A 9-block 2D arch with both-side FRP reinforcement

To illustrate the implementation of the above formulation, the collapse of a 9-block 2D arch with both-side FRP reinforcement

was studied as an example (Fig. 5). The load is applied to Block 2 and the boundary conditions at two supports are also regarded as frictional interfaces with double-side reinforcement. Properties of the FRP and the bricks are given in Table 1. The ultimate forces $F_{t,\max}$ and $F_{s,\max}$ were derived from the code CNR-DT200 [30] (Eq. (13)) and the peeling strength test [31] (Eq. (14)), respectively. b_f is the width of the FRP reinforcement, which is in our case the same as the width of the arch; peeling angle β defines the slope of the reinforcement with reference to the substrate in the peel-off process. We determine this value based on the experimental study reported in [31].

$$F^{ex}_{t,\max} = F^{in}_{t,\max} = F_{t,\max} = f_{bd} l_{ed} b_f = 29.7 \text{ kN} \tag{13}$$

$$F^{ex}_{s,\max} = F^{in}_{s,\max} = F_{s,\max} = E_f t_f b_f \tan^3\beta = 9.86 \text{ kN} \tag{14}$$

l_{ed} is the optimal bond length of the FRP suggested by CNR-DT200 [30], which derives directly from delamination considerations including the reinforcement type, fracture energy, and strength of the substrate material. Here it is worth noting that the problem of minimizing this optimal bond length l_{ed} required is not considered in light of a study of the optimal disposition of the reinforcement which will be presented after, because it would need to consider an additional variable, namely the dimension of the blocks.

The collapse behavior of the reinforced arch was predicted by both associated and non-associated formulations, solved through LP and SLP procedures, respectively. The results were compared with those of the arch without strengthening.

3.2. Collapse results

According to the results obtained with the associated formulation, the reinforcement as expected does not change the collapse mechanisms (Fig. 6a and Fig. 6c); indeed, all of the collapses exhibit a standard 4-hinge mechanism (S4H), with several segments of the thrust line being located outside the edges of the arch barrel due to the strengthening (Fig. 6c). The load multiplier after FRP strengthening is roughly 10 times higher than in the unreinforced case, which is obviously unrealistic from a technical point of view, despite fully justified not only by the simplistic assumptions of the model proposed (which does not account for the delamination of the strip from the support), but also for the fictitious enforcement of a failure driven by the formation of flexural hinges, promoted by the associativity of the flow rule. In the non-reinforcement case, the collapse results produced by non-associated limit analysis are in line with those from the associated formulation (Fig. 6a and Fig. 6b). However, the results become different when engaging the reinforcement (Fig. 6c and Fig. 6d). Instead of an S4H mechanism, the predicted collapse includes one hinge, one sliding-failure joint, and one hinge-sliding-mixed joint (HS1). The collapse load given by the associated formulation is also 21 % higher than that of the non-associated one, indicating that the associated analysis could provide an overestimated result, which in some cases is extremely high because of the impossibility to trigger sliding cracks.

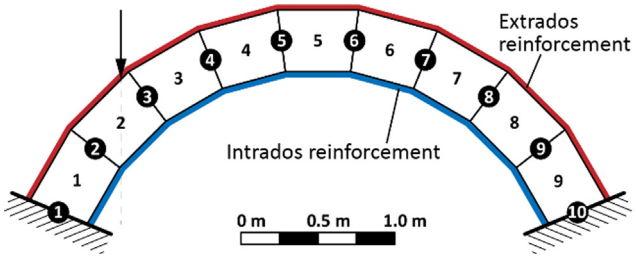

Fig. 5. Intrados and extrados strengthening scheme.

3.3. Parametric studies

This sub-section first investigates the influence of the friction angle φ (ranging from 20° to 40°) on the ultimate load (Fig. 7). The curve illustrates that the ultimate load for the collapse will grow if φ increases. With the increase of φ, three collapse mechanisms are successively present: local-sliding (LS), HS1, and S4H mechanism. The range of φ where the associated formulation predicts an S4H mechanism is wider than that of the non-associated one. This should be owing to the over restriction from the associated flow against the sliding at the joint. Note that the non-associated limit analysis always produces a conservative ultimate load. When φ drops, the overestimation of the associated formulation rises significantly. The maximum overestimation can reach 48.6 %.

The following parametric study concerns two extra cohesion forces provided by the FRP reinforcement. Intuitively, maximum tensile and sliding cohesions should be dependent on each other while we lack relevant contributions reporting such a relation. Thus, in the following, we assume them to be independent (ranging from 10^1 to 10^3 kN), attempting to cover all the possible cases. The results may also provide a reference for other types of innovative strengthening.

Let us now proceed to investigate the influence of the force $F_{t,\max}$ (called tensile-cohesive in the approach proposed for obvious reasons) on the collapse performance of the arch (Fig. 8). The ultimate load of the arch increases along with the growth of$F_{t,\max}$. When $F_{t,\max}$ increases, the associated limit analysis predicts the same S4H collapse mechanism while the collapse mechanisms produced from the non-associated side change from an S4H, HS1, to an LS one. This is because a higher tensile cohesion force will limit the separation of the joint. Comparatively, the sliding gives rise to less dissipation energy at the joint and thus becomes apt to happen. When $F_{t,\max}$ reaches a high level, the increase of the ultimate load given by non-associated analysis also slows down ascribed to such a change of collapse mechanism. The load multiplier produced by the non-associated limit analysis lay on the safer side compared to that of the associated one. The difference regarding the load

Table 1
Parameters for the FRP and the bricks.

FRP		Brick	
Thickness t_f [mm]	0.16	Width/Height/Depth [mm]	500/400/400
Young's Module E_f [GPa]	230	Strengthening depth b_f [mm]	400
Design bond strength f_{bd} [MPa]	0.202	Compressive strength f_{bc} [MPa]	8
Optimal bond length l_{ed} [mm]	366.872	Tensile strength f_{bt} [MPa]	0.8
Peeling angle β [°]	5	Friction angle for sliding φ [°]	30
		Half-length of joint tanη [mm]	200

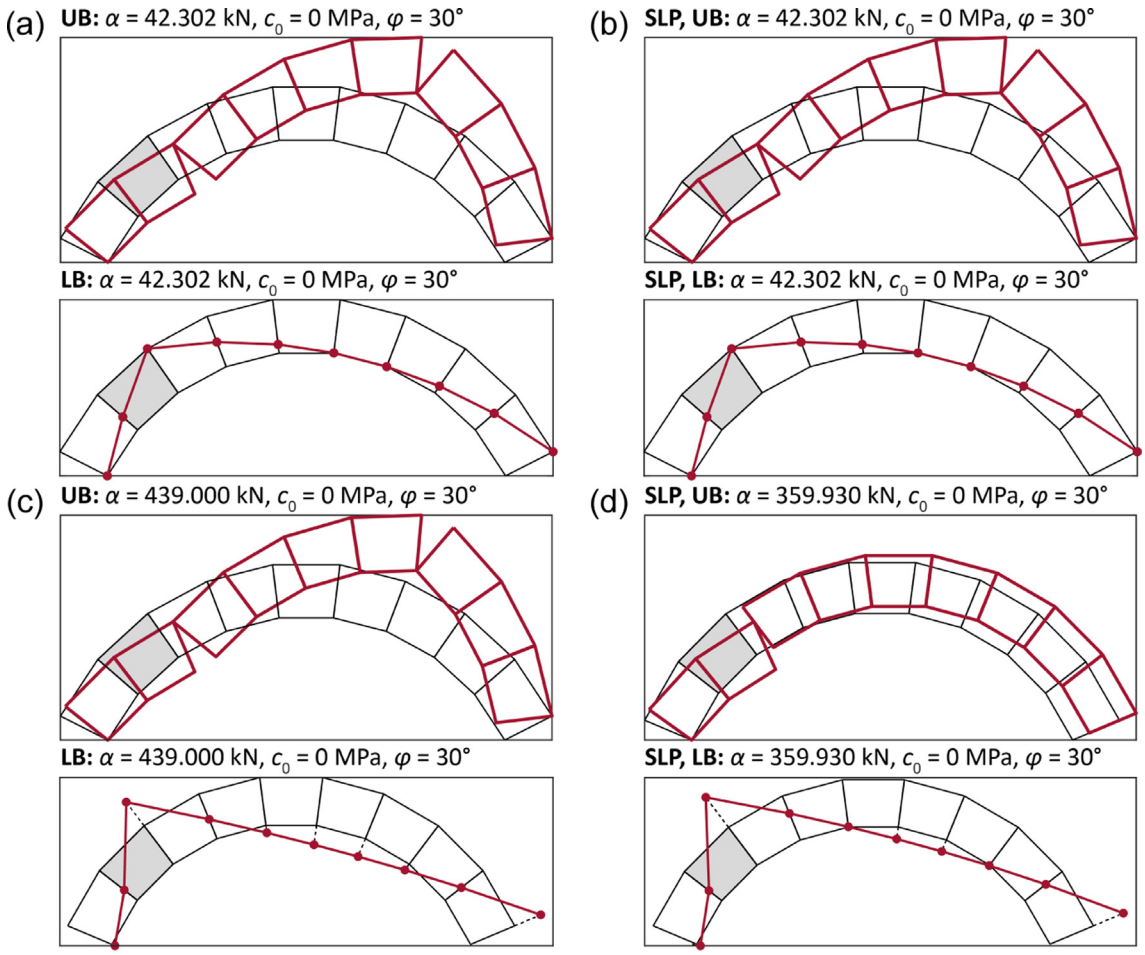

Fig. 6. Collapse results of the arch: (a) no reinforcement, associated flow; (b) no reinforcement, non-associated flow; (c) both-side reinforcement, associated flow; (d) both-side reinforcement, non-associated flow.

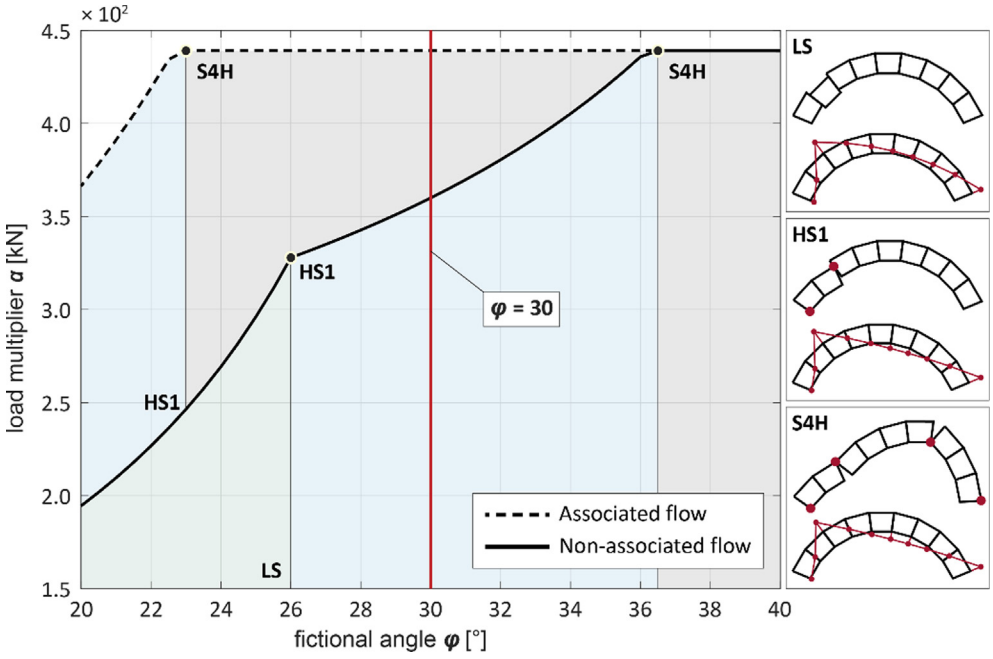

Fig. 7. Load multiplier α vs frictional angle φ: associated and non-associated flow, $F_{t,max}$ = 29.7 kN, $F_{s,max}$ = 9.86 kN.

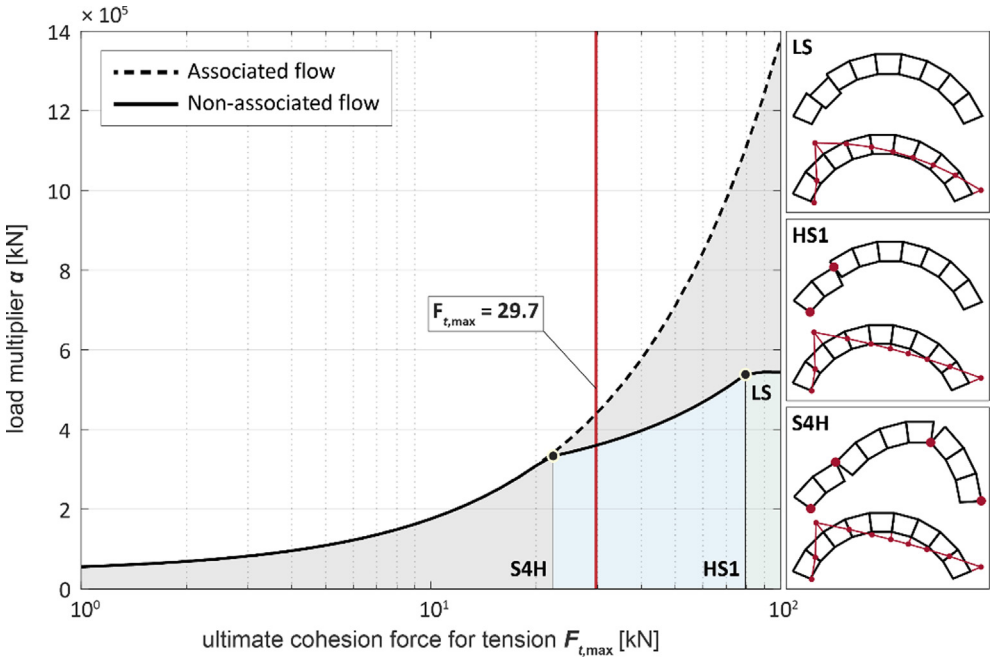

Fig. 8. Load multiplier α vs ultimate cohesion force for tension $F_{t,\max}$: associated and non-associated flow, φ = 30°, $F_{s,\max}$ = 9.86 kN.

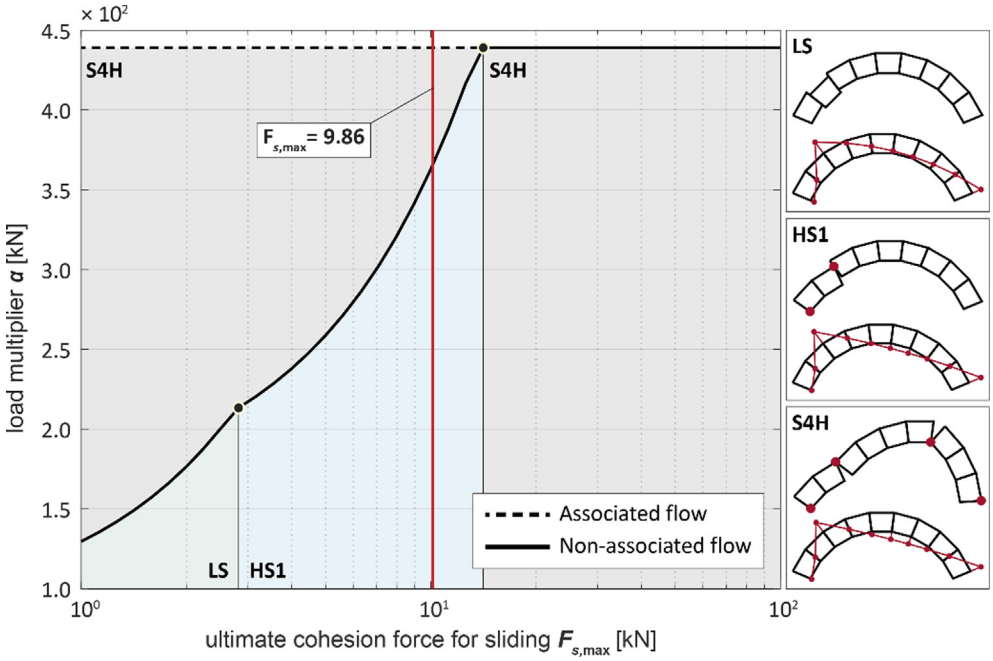

Fig. 9. Load multiplier α vs ultimate cohesion force for sliding $F_{s,\max}$: associated and non-associated flow, φ = 30°, $F_{t,\max}$ = 29.7 kN.

multiplier predicted by these two analyses grows along with the increase of$F_{t,\max}$. The maximum difference is about 60.7 %.

A parametric study regarding the sliding cohesion force $F_{s,\max}$ is then carried out (Fig. 9). The collapse of the arch employing an associated flow does not exhibit changes by changing the ultimate cohesion force. The load multiplier produced by the non-associated limit analysis significantly decreases once $F_{s,\max}$ drops, along with the change of the collapse mechanisms: from an S4H, HS1, to an LS mechanism. A higher sliding cohesion force will give rise to a larger sliding dissipation and thus limit the sliding at the joint. As a consequence, a large $F_{s,\max}$ will lead to an S4H collapse. Similarly, in this parametric study, employing the non-associated flow brings about a safer collapse load as well. The overestimation of the load multiplier increases when the $F_{s,\max}$ drops, with a maximum of 70.5 %, considering the results coming from the associated formulation.

Finally, we investigate the influence of different combinations of $F_{s,\max}$ and $F_{t,\max}$ on the collapse of the arch. As shown in Fig. 10, there exists a large area where the loads predicted by the associated formulation are overestimated. The fork enlarges when $F_{t,\max}/F_{s,\max}$ ratio increases, as it is visible observing the trend exhibited by Fig. 8 and Fig. 9. The maximum overestimation can reach 91 % for the associated prediction. Fig. 11 gives all the possible collapse mechanisms when the cohesion forces $F_{t,\max}$ and $F_{s,\max}$

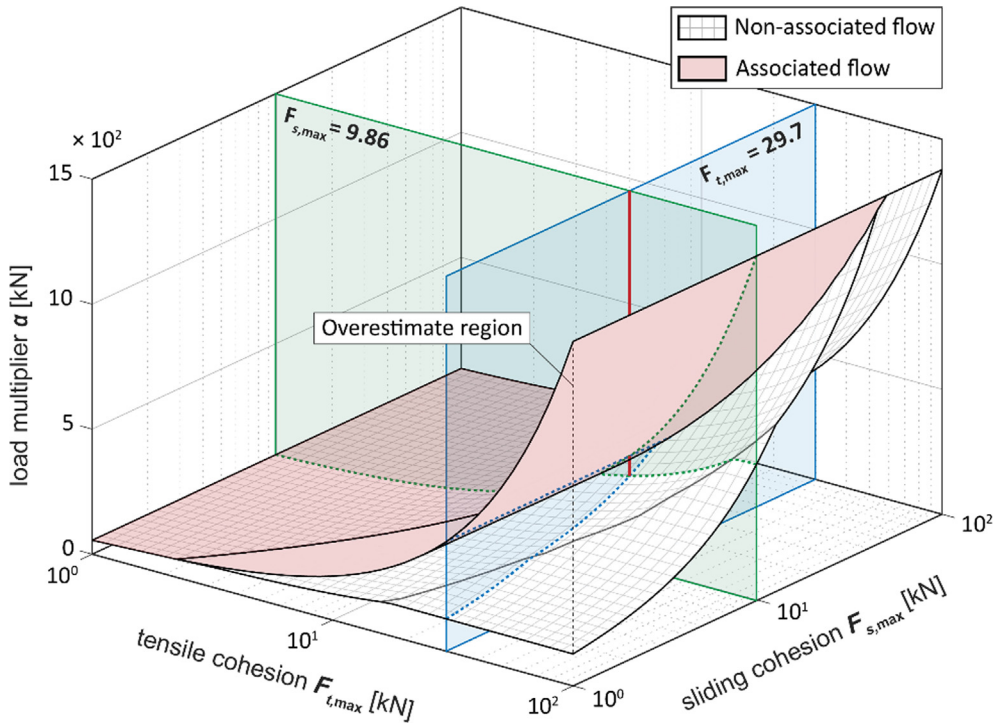

Fig. 10. Load multiplier α vs sliding cohesion $F_{s,max}$ and separation cohesion $F_{t,max}$: associated and non-associated flow, φ = 30°.

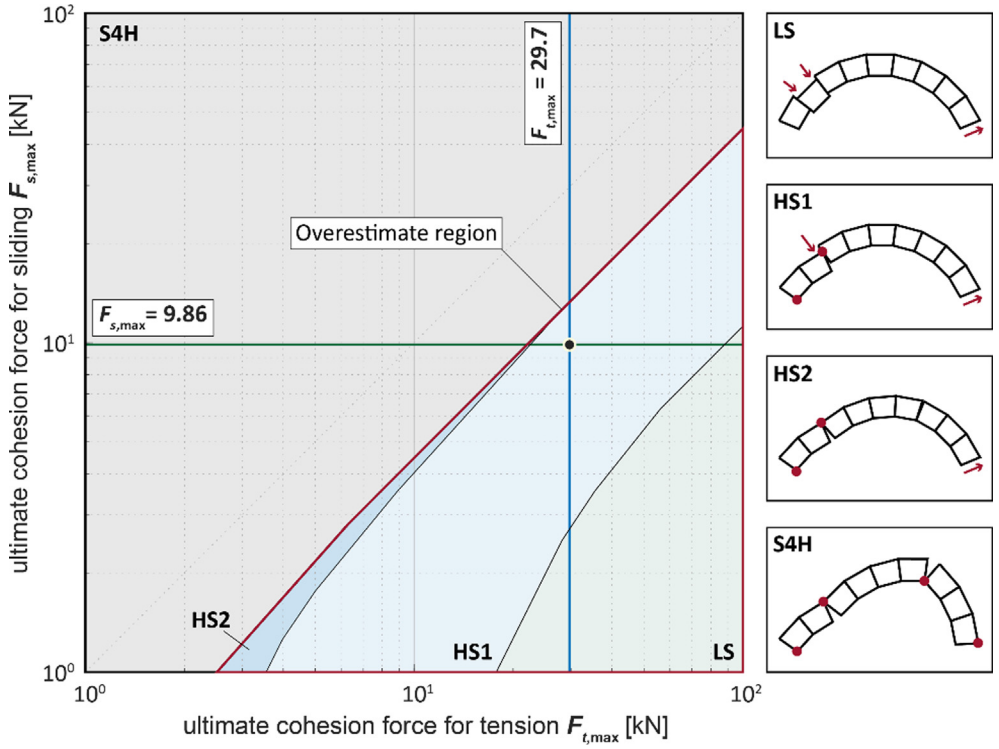

Fig. 11. Change of the collapse mechanism due to the variation of sliding cohesion $F_{s,max}$ and separation cohesion $F_{t,max}$: non-associated flow, φ = 30°.

vary. In the area where the collapse presents an S4H mechanism, the associated and non-associated formulations obviously coincide (because the flexural behavior is associated) and predict the same collapse load. Note that the whole diagonal lies in such "consistent prediction region", indicating that if the magnitude of the $F_{s,max}$ and $F_{t,max}$ grows in the same proportion, the associated and non-associated formulations will provide coincident results. In the case of a large $F_{t,max}/F_{s,max}$ ratio, sliding appears in the collapse mechanism. Besides the LS and the HS1 mechanism which have been mentioned in the previous parametric study, another hinge-sliding-mixed mechanism (HS2) is also found, occurring in a very narrow area of Fig. 11. This mechanism involves two hinges and

one sliding-failure joint. Along with the increase of the $F_{t,\max}/F_{s,\max}$ ratio, HS2, HS1, and LS mechanisms successively present. This trend is also in line with those already discussed for Fig. 8 and Fig. 9, varying separately $F_{s,\max}$ and$F_{t,\max}$. Fig. 12 illustrates the percentage difference in the collapse load produced by the two formulations under different cohesion force conditions. For HS2, HS1, and LS collapse, the difference with the associated prediction is 0.01–6.18 %, 1.76–51.7 %, and 51.7–90.7 %, respectively. In general, a large $F_{t,\max}/F_{s,\max}$ ratio will give rise to a more significant overestimation.

4. Cost-benefit study

In this section, we investigate the influence of different reinforcement layouts, aiming at optimizing the cost of the strengthening. Assuming a constant price of the strengthening material per meter, minimizing the total cost can be simply equivalent to minimizing its length, i.e. the number of the reinforced joint. As a consequence, a typical multi-objective optimization problem is derived, where the aim is to contemporarily maximize the load bearing capacity α and minimize the number of the reinforced joint N_{re}. Translating such request into mathematical programming, it is intended to solve the following associated LB/UB problems (15) and (16):

$$\begin{aligned}
&\underset{\alpha,\mathbf{x},\mathbf{z},N_{\text{re}},\mathbf{L}_{\text{re}}}{\text{minimize}} && -\alpha, N_{\text{re}} \\
&\text{subject to} && \mathbf{A}\mathbf{x} = \alpha\mathbf{f}_{\text{L}} + \mathbf{f}_{\text{D}} \\
& && \mathbf{N}\mathbf{x} - \mathbf{c}_0 - \mathbf{c}_m = \mathbf{z} \\
& && \mathbf{z} \le 0 \\
& && \Pi(\mathbf{L}_{\text{re}}, F_{t,\max}, F_{s,\max}) = \mathbf{c}_m \\
& && \Sigma(\mathbf{L}_{\text{re}}) = N_{\text{re}}
\end{aligned} \tag{15}$$

$$\begin{aligned}
&\underset{\mathbf{u},\mathbf{p},\mathbf{q},N_{\text{re}},\mathbf{L}_{\text{re}}}{\text{minimize}} && -\mathbf{f}_D^T\mathbf{u} + \mathbf{c}_0^T\mathbf{p} + \mathbf{c}_m^T\mathbf{p}, N_{\text{re}} \\
&\text{subject to} && \mathbf{f}_L^T\mathbf{u} = 1 \\
& && \mathbf{A}^T\mathbf{u} = \mathbf{N}^T\mathbf{p} \\
& && \mathbf{p} \ge 0 \\
& && \Pi(\mathbf{L}_{\text{re}}, F_{t,\max}, F_{s,\max}) = \mathbf{c}_m \\
& && \Sigma(\mathbf{L}_{\text{re}}) = N_{\text{re}}
\end{aligned} \tag{16}$$

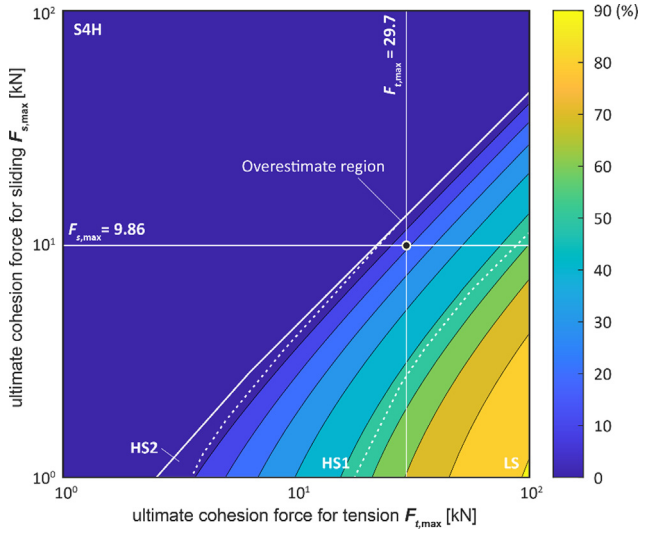

Fig. 12. Difference of the load multiplier α predicted by associated and non-associated formulation: variation of sliding cohesion $F_{s,\max}$ and tensile cohesion $F_{t,\max}$, φ = 30°.

$$\mathbf{L}_{\text{re}} = \begin{bmatrix} \mathbf{L}_{\text{re}}^{\text{in}} & \mathbf{L}_{\text{re}}^{\text{ex}} \end{bmatrix} = \begin{bmatrix} 1 & 1 & 1 & 1 & 1 & 1 & 1 & 1 & 1 & 1 \\ 0 & 0 & 0 & 0 & 0 & 0 & 0 & 0 & 0 & 0 \end{bmatrix}^T,$$
$$N_{\text{re}} = \Sigma(\mathbf{L}_{\text{re}}) = 10 \tag{17}$$

The constraint $\Pi(\mathbf{L}_{\text{re}}, F_{t,\max}, F_{s,\max}) = \mathbf{c}_m$ implies a mapping from the strengthening scheme and two ultimate cohesion forces to the spurious cohesion term $\mathbf{c}_m$, which is computable. $\mathbf{L}_{\text{re}}$ is a two-column bool-value matrix representing a specific strengthening scheme. The two values in row j indicate if the intrados and extrados of the joint j are reinforced or not, respectively (1 for true, 0 for false). Taking the 9-block arch presented in the last section as an example, we can represent the intrados reinforcement by $\mathbf{L}_{\text{re}}$ given in Eq. (17). N_{re} is the number of the reinforced joints, which can be calculated by summing all the elements in matrix $\mathbf{L}_{\text{re}}$ (denoted by $\Sigma(\mathbf{L}_{\text{re}}) = N_{\text{re}}$). For an intrados-reinforced 9-block arch, N_{re} is equal to 10 (see Eq. (17)). The non-associate solution was also obtained through the aforementioned SLP procedure, as illustrated in Algorithm 1.

The example of the 9-block 2D arch with the same dimensions and material parameters (see Table 1) assumed in section 3 is here re-considered. Due to the multiple objectives, the solution to the optimization problem is no longer a single value but a Pareto frontier must be determined. An enumeration strategy is employed to search for such a front. In every enumerating step, the number and location of the reinforcement at the intrados and extrados ($\mathbf{L}_{\text{re}}$ and N_{re}) are varied and then a new $\mathbf{c}_m$ is calculated. To reduce the enumeration time and in agreement with what occurs in practice applying a reinforcement, the following cases are investigated: (1) application of two strips, every-one with a certain length, one at the intrados and one at the extrados; (2) application of one strip with a certain length either at the intrados or at the extrados. In other words, the case of the application of fragmented strips is not considered and the reinforced joints are always assumed adjacent one each other, as shown in Fig. 13. The ultimate load for this new collapse problem scheme is solved through the proposed approach. Investigating all the possible permutations varying the position and length of the reinforcement, the cost-benefit chart depicted in Fig. 14 is obtained. An envelope curve can be found where two objective functions cannot be simultaneously minimized anymore.

Pareto fronts predicted by the associated and non-associated formulations coincide when the number of the reinforced joint is few (N_{re} < 6). According to intuition, these two Pareto fronts then branch when the number of the reinforced joints increases (N_{re} > 6). The difference is enlarged along with the increase of the reinforcement. In this case, a significant overestimation of the ultimate load is observed when the associated formulation is employed, which is consistent with the previous results.

Pareto front predicted by non-associated formulation presents two obvious plateaus, which is a consequence of the activation of different failure mechanisms. When the number of the reinforced joints (i.e. the reinforcement length) increases from 0 to 4, the

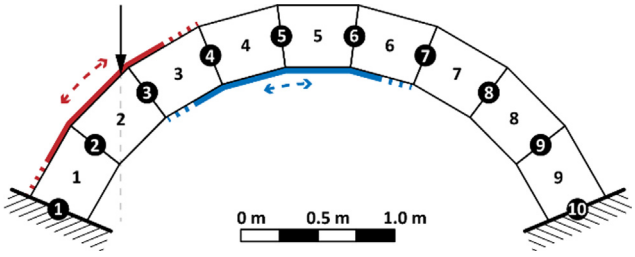

Fig. 13. Variation of the strengthening schemes considered in the cost-benefit study.

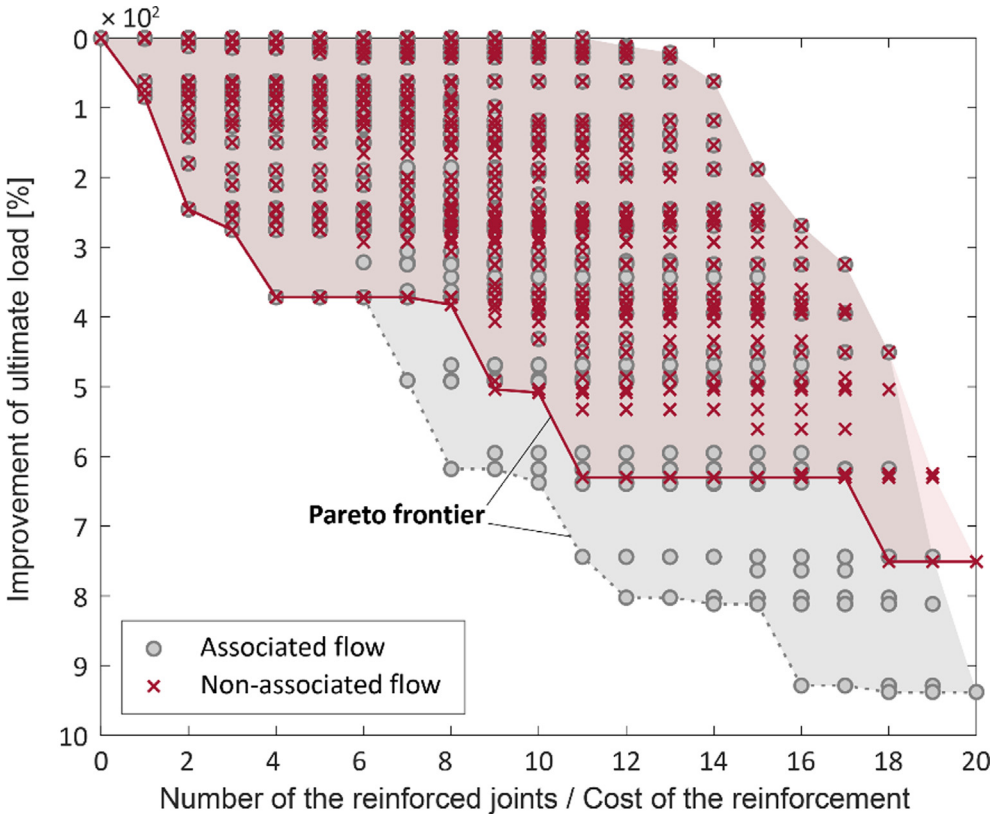

Fig. 14. Improvement of the ultimate load vs cost of the reinforcement, associated and non-associated formulation: variation of strengthening scheme, $\varphi = 30°$, $F_{t,max} = 29.7$ kN, $F_{s,max} = 9.86$ kN. The improvement is compared with the no-reinforcement case.

improvement of the ultimate load grows and reaches a first plateaus (371.7 %, $4 < N_{re} < 8$). After such plateau, the improvement starts to increase again and gets to the second plateaus (630.1 %, $11 < N_{re} < 17$). When the number of the reinforced joint is greater than 18, the improvement of the collapse load is obviously the maximum (750.9 %), but also the strengthening cost increases. In conclusion, it can be seen that when the number of the reinforced joints is larger than 11, the improvement of the ultimate load is about 84 % of the full-joint strengthening, which appears fully acceptable for practical purposes. Therefore, to reasonably guarantee a very high strengthening effect, it is recommended to reinforce at least one half of the joints.

5. Application on a real arch experimentally tested in-situ

To illustrate the possibility to apply the proposed method in large-scale problems, this section presents the collapse analysis of a real arch with a complex bond pattern, also taking into account spandrels. This case has been experimentally tested in-situ [32], including one unreinforced arch and one arch with Steel Reinforced Grout (SRG) reinforcement, with the same geometric properties. These two cases will both be analyzed in the following numerical studies and the results will be compared with the available testing data for further calibration and verification of the proposed approach.

The arch investigated in the following collapse analysis is completely modeled according to the one tested in [32], whose width is 250 mm, with a span of 3300 mm and a rise of 830 mm (Fig. 15). The thickness of this arch is 120 mm and the dimension of the bricks is approximately 250 × 120 × 55 mm. The horizontal distance between the loading point and the left springing is 556 mm, being consistent with the testing condition [32]. Two free sides and the bottom of the spandrel are regarded as frictional interfaces.

5.1. Unreinforced case

We first analyze the collapse of the unreinforced arch. Considering that in the previous analyses the initial cohesion c_0 (provided by mortar) is simply assigned to zero, here a sensitivity analysis on c_0 (from 0.001 to 0.03 MPa) is carried out. Results under two different friction conditions are presented ($\varphi = 22°$ and $\varphi = 30°$).

As shown in Fig. 16, the collapse load of the unreinforced arch increases with the growth of the initial cohesion. Such increase presents slight non-linearity, which is caused by the consideration of the spandrel. The trend of these curves also indicates that the collapse mechanism basically does not change when initial cohesion c_0 varies. Again, we observe the overestimation of the load multiplier from the associated formulation. Comparatively, such overestimation is more obvious in a large friction condition ($\varphi = 30°$). According to the experimental study [32], the collapse load of the unreinforced arch is 2.08 kN. Based on this value, we can calibrate the cohesions for both associated and non-associated formulations. All the calibrated cohesions remain within the range of 0.006–0.010 MPa, which are reasonable for a no-tension material. Note that the predicted loads are always conservative if we assume no initial cohesion, i.e. $c_0 = 0$ MPa.

Fig. 17 gives the collapse mechanism of the unreinforced arch under two friction conditions. Here we use the corresponding initial cohesion calibrated for the non-associated formulation. Presented collapse mechanisms are quite similar to the prior experimental results [32], which is generally a four-hinge collapse. Besides two hinges that appear in the middle of the arch, one hinge

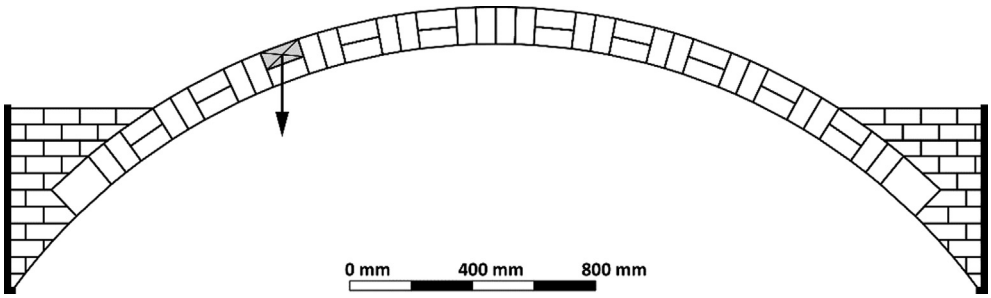

Fig. 15. Geometrical properties of the in-situ tested masonry arch.

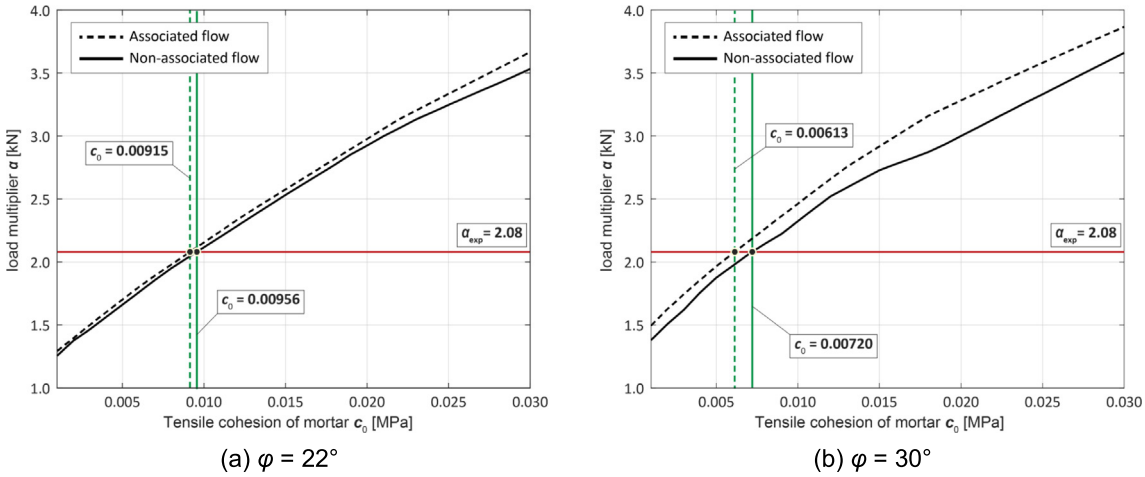

Fig. 16. Sensitivity analyses of initial cohesion c_0 under two friction conditions, unreinforced arch.

takes place near the springing under the right spandrel. In some cases, multiple hinges could be present at this location as well (see Fig. 17b). The last hinge, located at the bottom of the left spandrel, is not very obvious, also combining some sliding among the bricks. Note that the non-associated formulation predicts a small separation among the bricks at the right spandrel, which should be more close to reality. However, the overestimation of the associated formulation is acceptable in this case (1.70–4.67 %, compared with the associated prediction) because sliding happening in the collapse is very localized.

5.2. SRG-Reinforced case

This subsection analyzes the collapse of the same arch with SRG reinforcement. Referring to the experimental study [32], we only consider an extrados reinforcement here, including two different

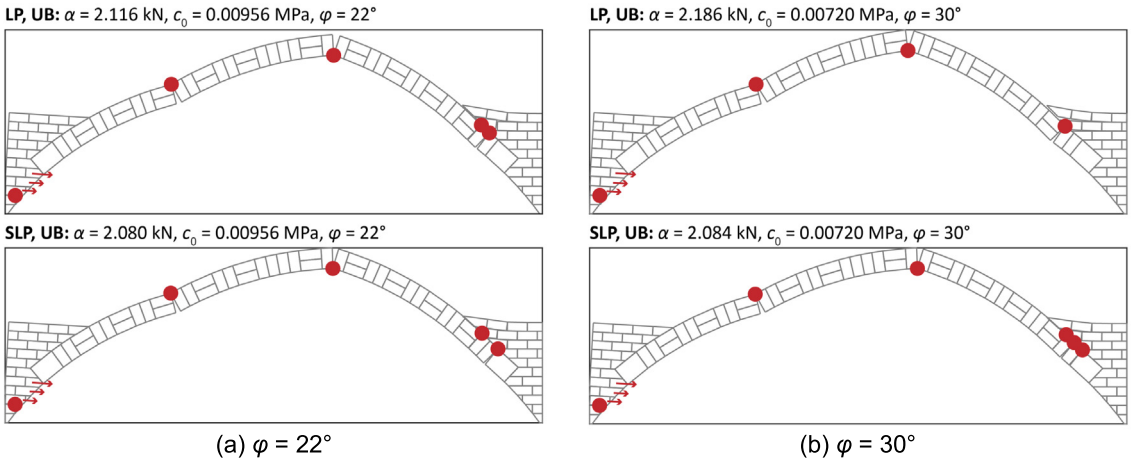

Fig. 17. Collapse mechanisms of the unreinforced arch under two friction conditions.

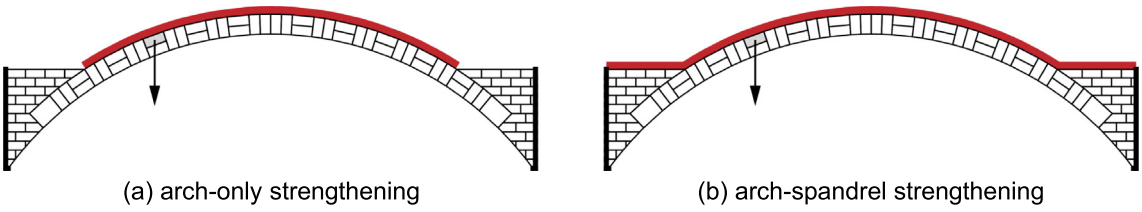

Fig. 18. Two extrados strengthening schemes taken into account in the following collapse analyses.

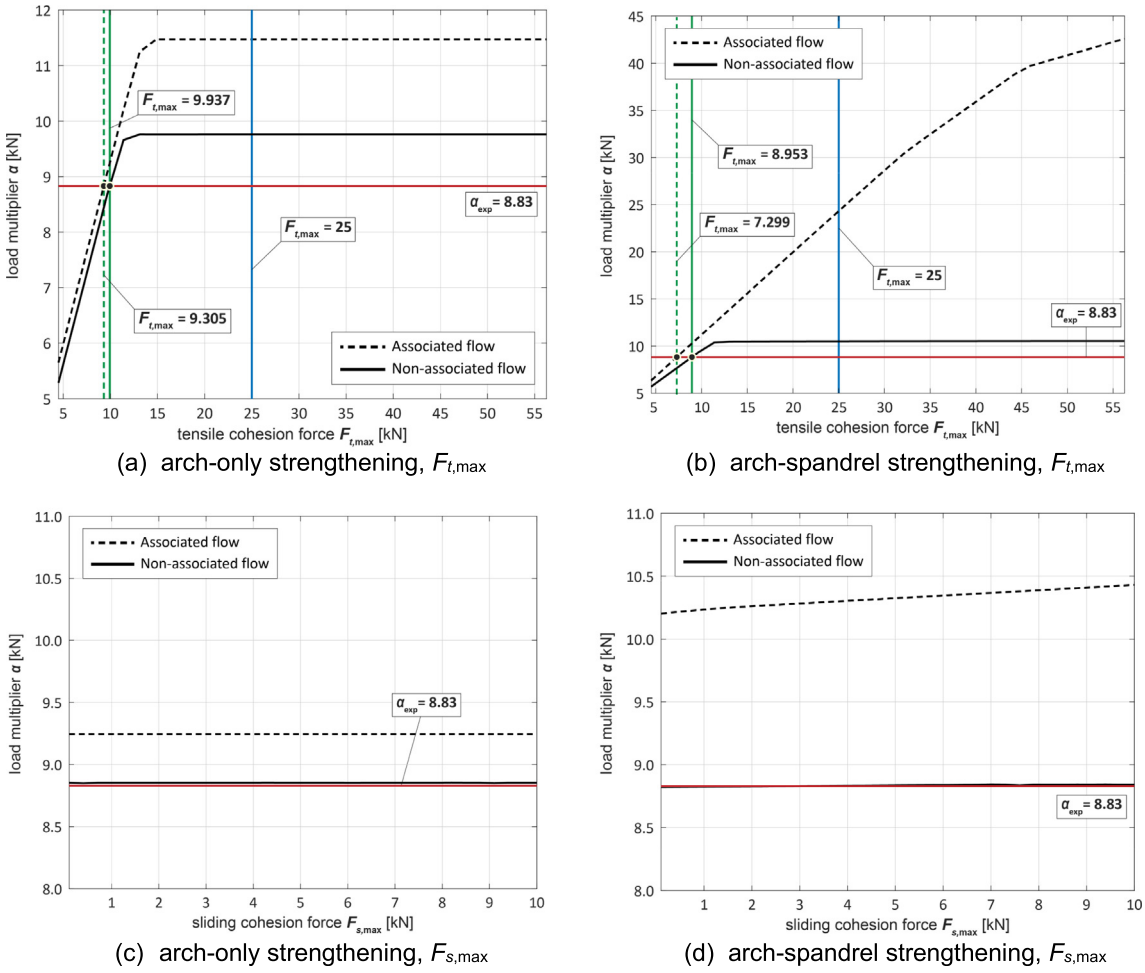

Fig. 19. Sensitivity analyses of tensile cohesion $F_{t,\max}$ and sliding cohesions $F_{s,\max}$, SRG-reinforced arch, $\varphi = 22°$.

schemes: (1) strengthening applied at the extrados but only on the arch barrel (Fig. 18a); (2) strengthening at the extrados applied on both arch and spandrels (Fig. 18b). According to the calibrated results presented in [33], in the following analyses, the friction angle of the bricks is fixed to 22°. Sensitivity analyses on the two cohesions forces provided by the SRG are carried out. The tensile cohesion of the SRG is calculated basing on Eq. (18).

$$F_{t,\max}^{\mathrm{ex}} = \sigma_{\mathrm{r}} t_{\mathrm{eq}} b_{\mathrm{f}},\ F_{t,\max}^{\mathrm{in}} = 0 \tag{18}$$

Where σ_{r} is the debonding strength of the SRG, which should range from 600 to 750 MPa according to the material test reported in [32]. t_{eq} is the equivalent thickness of the SRG. In the sensitivity analyses, we vary it from 0.03 to 0.3 mm. b_{f} is the width of the reinforcement, which is, in this case, the same as the width of the arch.

We first present the sensitivity analysis on tensile cohesion $F_{t,\max}$. Because the peeling test for the SRG is not presented in [32], as a simplification, we stick the sliding cohesion $F_{s,\max}$ to 1/3 of $F_{t,\max}$, referring to the proportion of these two forces discussed in section 3. The collapse load of the arch with arch-only strengthening first increases with the growth of the tensile cohesion and then reaches a plateau (Fig. 19a). The trend of the curves predicted by associated and non-associated formulations are in line one each other while the collapse load at the plateau is different. At this plateau, the overestimation of the load multiplier due to the employment of an associated flow also reaches the maximum (14.8 % of increase). In the arch-spandrel strengthening case, curves of associated and non-associated solutions exhibit different trends when $F_{t,\max}$ is large: the non-associated prediction does not grow anymore while the associated one continuously increases (see Fig. 19b). As a result, the overestimation of the associated formulation becomes very significant (maximum 75.3 %) when the tensile cohesion is large.

Similarly, we can calibrate the tensile cohesion from the experimental result (8.83 kN referring to [32]). Calibrated tensile cohe-

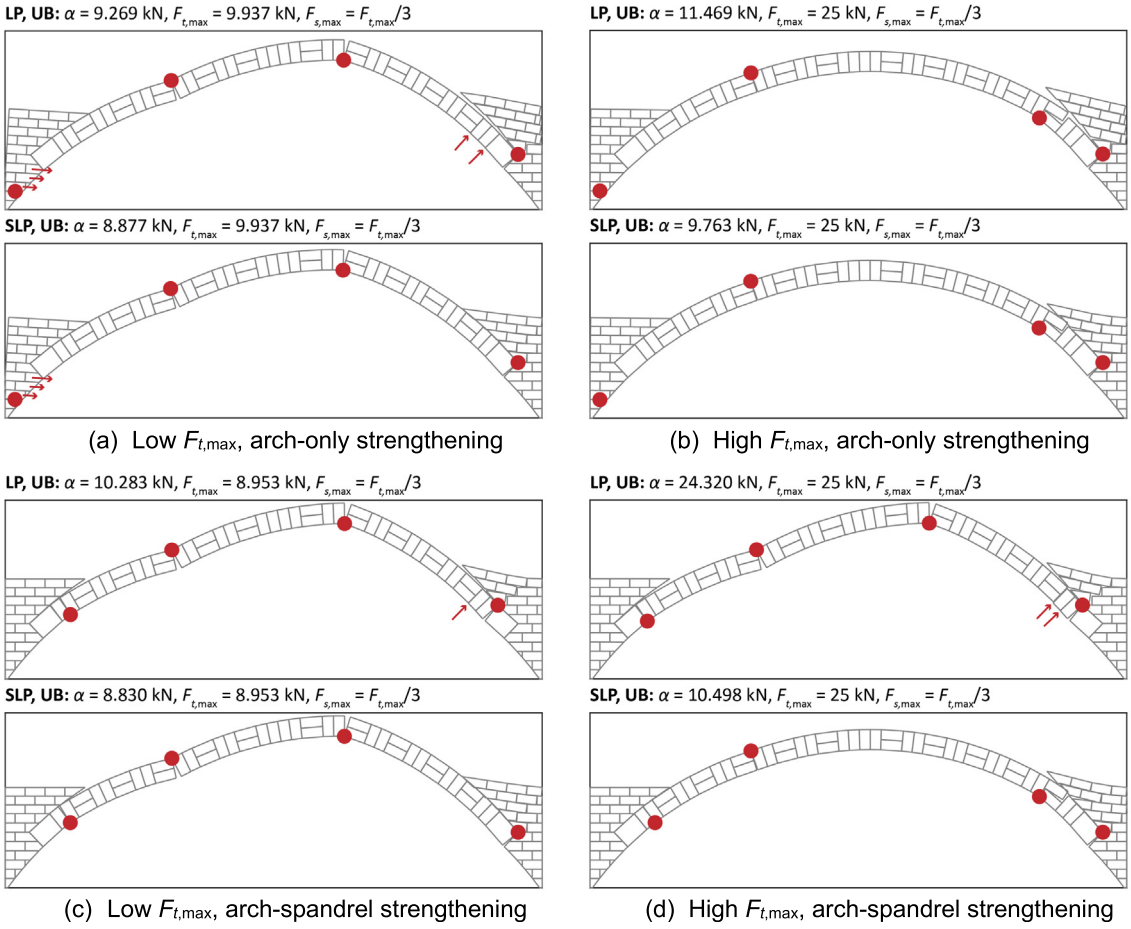

Fig. 20. Collapse mechanism of the SRG-reinforced arch with two different tensile cohesion.

sions are indicated with green lines in Fig. 19a and Fig. 19b. Comparatively, the calibrated tensile cohesion in the arch-only strengthening case is higher. All these cohesions stay within the range 7–10 kN, which should be reasonable for SRG reinforcements. Then, we carry out the sensitivity analysis on the sliding cohesion $F_{s,\max}$ (Fig. 19c and Fig. 19d). In this sensitivity analysis, we assign the tensile cohesion equal to the value calibrated with the non-associated formulation (corresponding to the two strengthening schemes). The curves indicate that the load multipliers are basically not influenced by the change of $F_{s,\max}$. Only for the arch-spandrel strengthening arch, the associated solution slightly grows when $F_{s,\max}$ rises (see Fig. 19d).

The occurrence of the plateau stage in the curves of the sensitivity analysis on $F_{t,\max}$ should indicate a change in the collapse mechanism. Therefore, let us finally investigate how the collapse mechanism changes when $F_{t,\max}$ varies. The collapse mechanisms at two different levels of tensile cohesion are presented: (1) tensile cohesions calibrated for the non-associated formulation ($F_{t,\max}$ = 9.937 and 8.953 kN for arch-only and arch-spandrel strengthening, respectively), which is located on the increasing stage of the curve, and (2) $F_{t,\max}$ = 25 kN, located at the plateau stage (as noted in Fig. 19a and Fig. 19b). Note here that we still assign a sliding cohesion $F_{s,\max}$ equal to 1/3 of $F_{t,\max}$.

In the case of arch-only reinforcement, when the tensile cohesion increases, the location of one hinge changes: one intrados hinge at the middle part of the arch moves to the ring under the right spandrel (compare Fig. 20a and Fig. 20b). Consequently, only one extrados hinge remains within the reinforced span. This hinge opens at the intrados while no SRG reinforcement is applied at this side. Thus, for such a collapse mechanism, the growth of the tensile cohesion does not enhance the collapse load anymore, which explains the occurrence of the plateau stage in Fig. 19a. Associated and non-associated formulations predict similar collapse mechanisms under two different tensile cohesion conditions. Only the associated solution presents large separations among the bricks (in particular in the right spandrel in Fig. 20a and Fig. 20b, LP). For the arch-spandrel strengthening, associated and non-associated solutions are consistent under a low tensile cohesion condition while these two solutions become different when the $F_{t,\max}$ increases. Like the arch-only-reinforced case, when the tensile cohesion is high, the collapse mechanism produced by the non-associated formulation exhibits only one extrados hinge in the reinforced area (Fig. 20d, SLP). Therefore, the variation of the $F_{t,\max}$ does not change the ultimate load. While in the associated solution, one intrados hinge appears within the reinforced area (Fig. 20d, LP). The collapse load keeps increasing with the growth of $F_{t,\max}$. As a result, the overestimation of the associated formulation becomes significant in this case. Note that the sliding that happens in such collapses is not obvious, a feature which explains why the load multiplier is not influenced by the change of the sliding cohesion (see Fig. 19c and Fig. 19d). The corresponding experimental result is closer to the mechanism presented in Fig. 20b.

6. Conclusions

We have proposed a modeling strategy for including the strengthening effect in the heterogeneous limit analysis of masonry arches with infinitely resistant blocks. It relies into a stan-

dard heterogeneous approach, i.e. without the use of overlaying new elements; in particular, a "spurious cohesion" term was added to the constraint of the joint reduced to interface, defining new constitutive laws. Based on such approach, a collapse analysis of a 2D arch with FRP reinforcement was carried out as a benchmark example, followed by several parametric studies and a cost-benefit study. Employing this approach, we also analyzed the collapse of a real arch experimentally tested in-situ for further verification.

As mentioned in the introduction, recent works have almost always neglected the non-associated sliding when analyzing the collapse of reinforced arches. Nevertheless, the results of this paper illustrate that such a disregard could lead to an inaccurate prediction of the collapse. The collapse mechanism of common arches with reinforcement reported in recent works is primarily a four-hinged one S4H (see [19,22] for instance, and Fig. 6a). On the contrary, according to both experimental observations (e.g. [34]) and the results of this study, the presence of the reinforcement most likely is responsible for a considerable change of the collapse mechanism. Employing associated limit analysis, such failure modes are hardly predictable, but once involving non-associated sliding, it is possible to obtain mixed collapse mechanisms with the contemporary presence of flexural hinges and sliding interfaces (HS1 and HS2), as well as mechanisms characterized by pure-sliding (LS). Moreover, as reported also in other existing literature [11,12,17], an associated limit analysis could lead in some selected cases to an overestimation of the ultimate load even in absence of reinforcement, which is also in line with the results of this study. This overestimation becomes in several cases critical when accounting for the reinforcement in the analyses. Generally, according to the analysis of the 9-block arch, a large $F_{t,\max}/F_{s,\max}$ ratio tends to bring about more sliding in the collapse, and the overestimation of the collapse load using classic limit analysis becomes more significant. The simulation of the in-situ tested arch also indicates that even though no sliding appears in the collapse, the locations of the hinges predicted by the associated and non-associated formulation will be different when $F_{t,\max}/F_{s,\max}$ ratio is large. The overestimation of the associated solution will become obvious in this case. From the cost-benefit study, such overestimation also becomes extremely high when the number of reinforced joints increases. Obviously, the results of the presented cases also indicate that the ultimate load predicted by the associated and non-associated formulations will be close if the two predicted collapse mechanisms are the same. In this case, the associated formulation can still be used to avoid an iterative search of the collapse state through an SLP procedure. However, if relevant in-situ tests are lacking or engineering experience is insufficient, this criterion is difficult to be judged only by implementing an associated limit analysis. Therefore, in general, we would recommend directly conducting a non-associated limit analysis for a more accurate prediction.

When applying the proposed modeling strategy, the choice of the two ultimate cohesion forces, $F_{t,\max}$ and$F_{s,\max}$, is crucial being their influence on the results quite high. Generally, the tensile cohesion force $F_{t,\max}$ is comparatively easier to be determined, because extensive debonding tests have been carried out for different types of strengthening materials in recent works (e.g. [35–40]). $F_{t,\max}$ can be easily stemmed from the debonding strength. For FRP reinforcement, for instance, the code of practice CNR-DT200 has also provided clear guidance to calculate such resistance [30]. On the other hand, the sliding cohesion force $F_{s,\max}$ should be calculated based on the peeling strength of the bond between reinforcement and substrate. However, the peeling mechanism of the interface between different reinforcements and masonry is still object of jeopardized investigation in the literature, especially for curved substrates like arches. Relevant peeling tests have been scarcely reported in recent contributions and the results turned out to appear rather scattered [31,40]. A detailed parametric study varying in a wide range the ultimate sliding cohesion force $F_{s,\max}$ can be useful to have a better insight into all possible collapse modes triggering, in case that a reliable peeling strength is not available experimentally.

As far as the cost-benefit study is concerned, according to the Pareto fronts predicted by the non-associated formulation, it can be deduced that roughly-one half of the joints should be reinforced to guarantee an acceptable strengthening effect at the same time reducing installation costs.

In the collapse analysis of the in-situ tested arch, the predicted collapse mechanism is quite close to the experimental results, for both unreinforced and reinforced arches. The prediction of the collapse load should also be justified because all the calibrated parameters remain in a reasonable range. Note that if we assume a zero initial cohesion for masonry, the proposed code always predicts a safe load multiplier compared with the experimental results.

On the basis of the foregoing results and discussion, it may be affirmed that the proposed approach can successfully simulate the enhancement of the ultimate load carrying capacity and the change of the collapse mechanism in masonry arches after strengthening.

However, the limitations of the proposed approach still exist. To give a fast prediction, the reinforcement is modeled only in an implicit manner. Thus, the failure mechanism between the reinforcement layer and substrate cannot be deduced. A detailed load–displacement description for the whole collapse process is also absent because the proposed code is based on limit analysis. On top of that, although a non-associated solution is more realistic than an associated one, we cannot confirm if the minimum load multiplier is predictable by the SLP procedure. At least in principle, the involvement of the non-associativity can give rise to multiplicities of the solution (many contributions have reported this issue, see [11–12,41]). The SLP procedure can give the solution with a minimum load multiplier only in a simple two-block system [17] while for a more complex block system no theoretical study is available to guarantee the minimization. Therefore, the proposed approach still requires more verifications from experimental and numerical contributions.

Besides further verifications and calibrations of the proposed approach, future work will concern extending this approach to solve 3D geometric problems because up to now it can only deal with 2D cases. In this manner, the analysis of reinforced skew arches could be possible. Analyzing the arch with different geometries and the collapse with non-zero dilations will also be postponed to our future work. Finally, as we discussed above, cohesion forces provided by the reinforcement are difficult to be derived if relevant material tests are not available. For this sake, we will investigate possible analytical formulations to calculate these parameters. These formulations should predict the extra cohesion forces basing on the actual debonding of the reinforcement that can be determined with standard tests, also considering the role played by the curvature of the substrate.

Data availability

Data will be made available on request.

Declaration of Competing Interest

The authors declare that they have no known competing financial interests or personal relationships that could have appeared to influence the work reported in this paper.

Acknowledgments

Yiwei Hua would like to thank the financial support from China Scholarship Council (CSC) under the grant CSC No. 202108320019.

Appendix A

This appendix first presents a detailed deduction of the formulation of the failure surface after the reinforcement. Considering a contact shown in Fig. 2c, the force vector at the contact can be decomposed to three components along$\bar{n}$,$\bar{s}$, and $\bar{m}$ (Fig. 2d). Now we deduce the constraints that these three resultants should obey at the interface. According to the equivalence of the force, the relations between the real force (n, s) and these three resultants, including the extra forces provided by the reinforcement layer as well as the initial cohesion c_0, are given as follows. A and t are the area and length of the contact, respectively.

$$\bar{n} = n + F_t^{\text{in}} + F_t^{\text{ex}} + c_0 A \tag{19}$$

$$\left.\begin{aligned} \bar{s} &= s + F_s^{\text{in}} + F_s^{\text{ex}},\ s \geq 0 \\ \bar{s} &= s - F_s^{\text{in}} - F_s^{\text{ex}},\ s < 0 \end{aligned}\right\} \Rightarrow \left|\bar{s}\right| = |s| + F_s^{\text{in}} + F_s^{\text{ex}} \tag{20}$$

$$\bar{m} = n \cdot e + F_t^{\text{in}} \tan\eta - F_t^{\text{ex}} \tan\eta,\ \tan\eta = \frac{t}{2} \tag{21}$$

Substitute n in Eq. (21) by Eq. (19), the eccentricity of the normal force n can be represented by $\bar{n}$ and $\bar{m}$ (Eq. (22)). To meet the static condition, no rotation should happen at this contact. Thus, the acting point of the normal force should remain within the section. Then we get Eq. (23) constraining interfacial resultants $\bar{n}$ and$\bar{m}$.

$$e = \frac{\bar{m} - F_t^{\text{in}} \tan\eta + F_t^{\text{ex}} \tan\eta}{\bar{n} - F_t^{\text{in}} - F_t^{\text{ex}} - c_0 A} \tag{22}$$

$$|e| \leq \frac{t}{2} \Rightarrow \left|\frac{\bar{m} - F_t^{\text{in}} \tan\eta + F_t^{\text{ex}} \tan\eta}{\bar{n} - F_t^{\text{in}} - F_t^{\text{ex}} - c_0 A}\right| \leq \tan\eta \tag{23}$$

Here we use tanη to represent the half height of the section. η is the friction angle regarding the rotation, defining the limits of the moment with respect to the normal force at the contact.

The constraints regarding $\bar{n}$ and $\bar{s}$ can be derived from the classical Coulomb friction model, as shown in the left of Eq. (24). Substituting n and s through Eq. (19) and Eq. (20), we can get the formulation at the right side. φ is the friction angle referred to sliding, given the limits of the shear force.

$$\begin{aligned} & n \tan\varphi + |s| \leq 0 \\ & \quad \Rightarrow \left(\bar{n} - F_t^{\text{in}} - F_t^{\text{ex}} - c_0 A\right) \tan\varphi + \left|\bar{s}\right| - F_s^{\text{in}} - F_s^{\text{ex}} \\ & \quad \leq 0 \end{aligned} \tag{24}$$

Both Eqs. (23) and (24) can be equivalent to a pair of inequality constraints. The reinforcement will reach maximum strength when the interface is about to fail. Thus, we can simply substitute the four extra forces (F_t^{in},F_t^{ex},F_s^{in}, and F_s^{ex}) with their corresponding strength.

$$\begin{cases} \bar{n} \sin\eta + \bar{m} \cos\eta - \underbrace{2F_{t,\max}^{\text{in}} \sin\eta}_{c_m^{r+}} - \underbrace{c_0 A \sin\eta}_{c_0^{r+}} \leq 0, \\ \qquad \bar{m} - F_{t,\max}^{\text{in}} \tan\eta + F_{t,\max}^{\text{ex}} \tan\eta \geq 0 \\ \bar{n} \sin\eta - \bar{m} \cos\eta - \underbrace{2F_{t,\max}^{\text{ex}} \sin\eta}_{c_m^{r-}} - \underbrace{c_0 A \sin\eta}_{c_0^{r-}} \leq 0, \\ \qquad \bar{m} - F_{t,\max}^{\text{in}} \tan\eta + F_{t,\max}^{\text{ex}} \tan\eta < 0 \end{cases} \tag{25}$$

$$\begin{cases} \bar{n} \sin\varphi + \bar{s} \cos\varphi - \underbrace{\left(\left(F_{t,\max}^{\text{in}} + F_{t,\max}^{\text{ex}}\right) \sin\varphi + \left(F_{s,\max}^{\text{in}} + F_{s,\max}^{\text{ex}}\right) \cos\varphi\right)}_{c_m^{s+}} \\ \qquad - \underbrace{c_0 A \sin\varphi}_{c_0^{s+}} \leq 0,\ \bar{s} \geq 0 \\ \bar{n} \sin\varphi - \bar{s} \cos\varphi - \underbrace{\left(\left(F_{t,\max}^{\text{in}} + F_{t,\max}^{\text{ex}}\right) \sin\varphi + \left(F_{s,\max}^{\text{in}} + F_{s,\max}^{\text{ex}}\right) \cos\varphi\right)}_{c_m^{s-}} \\ \qquad - \underbrace{c_0 A \sin\varphi}_{c_0^{s-}} \leq 0,\ \bar{s} < 0 \end{cases} \tag{26}$$

As a consequence, inequalities (25) and (26) define the failure surfaces, taking into account the reinforcement, referred to rotation and sliding, respectively. Rewriting them in matrix form, we can obtain Eq. (2). The components in the two cohesion terms $\mathbf{c}_0$ and $\mathbf{c}_m$ (given in Eqs. (3) and (4)) correspond to the constant terms in Eqs. (25) and (26).

In addition, we explain more about the basic theory of associated limit analysis. Standard formulations include both Lower Bound (LB) and Upper Bound (UB) theories, describing the collapse condition from statics and kinematics viewpoints, respectively. LB formulation (Eq. (5)) maximizes the external load multiplier α in the condition of equilibrium and constitutive law. The constitutive law defines the failure surface where the joint resultant state should not exceed, as discussed in section 2. Here we elaborate on the deduction of the equilibrium condition (first constraint in Eq. (5)). This condition describes the relation between the interface resultants $\times$ and the force applied at the centroid of the block (Fig. 21a).

Considering block i, such an equilibrium can be expressed by Eq. (27). Th right side of the equation represents the external force acting at the centroid of block i, where $\mathbf{f}_D^i$ and $\mathbf{f}_L^i$ are vectors collecting all the dead and live loads applied to this block. sgn(x) is the sign function. At the left side, the matrix $\mathbf{A}_j^i$ transforms the interface resultant $\mathbf{x}_j$ to the equivalent centroid-acting forces, and the sum of these forces for all the joint j associated with block i is equal to the external force (right side). More details can be found in [12,16,41].

$$\sum_{j \in J_i} \text{sgn}\left(\mathbf{r}_j^i \mathbf{e}_n^j\right) \mathbf{A}_j^i \mathbf{x}_j = \alpha \mathbf{f}_L^i + \mathbf{f}_D^i,\ J_i = \{j | \text{joint } j \text{ is assocaited with block } i\} \tag{27}$$

The contains in the vectors and matrix in Eq. (27) are given in Eq. (28). Here,$\bar{n}_j$,$\bar{s}_j$, and $\bar{m}_j$ are the normal force, shear force, and moment acting at the interface j; F_{Lx}^i and F_{Ly}^i are the live load in $\times$ and y direction. In this paper, we only consider vertical loads, thus we assign $F_{Lx}^i = 0$ and$F_{Ly}^i = -1$. W_i represents the dead load of block i, i.e. its weight.

$$\mathbf{A}_j^i = \begin{bmatrix} \mathbf{e}_n^j \mathbf{e}_x & \mathbf{e}_t^j \mathbf{e}_y & 0 \\ \mathbf{e}_n^j \mathbf{e}_x & \mathbf{e}_t^j \mathbf{e}_y & 0 \\ -\mathbf{e}_t^j \mathbf{r}_j^i & \mathbf{e}_n^j \mathbf{r}_j^i & 1 \end{bmatrix},\ \mathbf{x}_j = \begin{bmatrix} \bar{n}_j \\ \bar{s}_j \\ \bar{m}_j \end{bmatrix},\ \mathbf{f}_L^i = \begin{bmatrix} F_{Lx}^i \\ F_{Ly}^i \\ 0 \end{bmatrix},\ \mathbf{f}_D^i = \begin{bmatrix} 0 \\ -W_i \\ 0 \end{bmatrix} \tag{28}$$

The UB formulation (Eq. (6)) minimizes the total power of the structure, defined by the sum of the potential power of the blocks $-\mathbf{f}_D^T \mathbf{u}$ and the dissipation power at the interface $\mathbf{c}_0^T \mathbf{p} + \mathbf{c}_m^T \mathbf{p}$ (see Eq. (6)). Since we have discussed the flow rule in section 2, more details about the geometric compatibility condition (first constraint in Eq. (6)) are given here. This condition calculates the discontinuous velocities at each joint (j for example), collected in $\mathbf{q}_j$, based on the centroid velocity of the adjacent blocks $\mathbf{u}_i$ (Fig. 21b). The transposed matrix $\mathbf{A}_j^i$ projects the centroid compo-

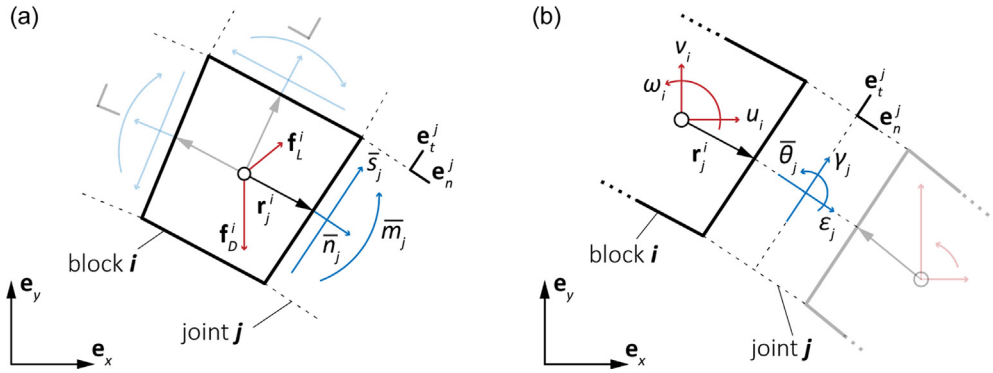

Fig. 21. Diagram of (a) equilibrium condition and (b) geometric compatibility condition.

nents from the global coordinate ($\mathbf{e}_x, \mathbf{e}_y$) to the local coordinate of the joint j ($\mathbf{e}_n^j, \mathbf{e}_t^j$), and the sum of these projected components can define the discontinuous velocities at this joint (Eq. (29)).

$$\sum_{i\in I_j} \operatorname{sgn}\left(\mathbf{r}_j^i \mathbf{e}_n^j\right)\left(\mathbf{A}_j^i\right)^T \mathbf{u}_i = \mathbf{q}_j,\ I_j = \{i|\text{block } i \text{ is associated with joint } j\} \tag{29}$$

Eq. (30) gives the contains in the vectors $\mathbf{q}_j$ and $\mathbf{u}_i$. Here, u_i, v_i, and$\bar{\omega}_i$, are the horizontal, vertical, and rotational velocities at the centroid of block i; ε_j, γ_j, and $\bar{\theta}_j$ are the horizontal, vertical, and rotational discontinuous velocities at the joint j.

$$\mathbf{u}_i = \begin{bmatrix} u_i \\ v_i \\ \bar{\omega}_i \end{bmatrix},\ \mathbf{q}_j = \begin{bmatrix} \varepsilon_j \\ \gamma_j \\ \bar{\theta}_j \end{bmatrix} \tag{30}$$

Assembling Eqs. (27) and (28) for all the joints and blocks, we can get the equilibrium and geometric compatibility constraints in the LB and UB formulation, respectively.

References

[1] Giordano E, Mendes N, Masciotta MG, Clementi F, Sadeghi NH, Silva RA, et al. Expeditious damage index for arched structures based on dynamic identification testing. Constr Build Mater 2020;265:. https://doi.org/10.1016/j.conbuildmat.2020.120236120236.

[2] Sarhosis V, Forgács T, Lemos JV. A discrete approach for modelling backfill material in masonry arch bridges. Comput Struct 2019;224:. https://doi.org/10.1016/j.compstruc.2019.106108106108.

[3] Chen S, Ferrante A, Clementi F, Bagi K. DEM analysis of the effect of bond pattern on the load bearing capacity of barrel vaults under vertical loads. Int J Mason Res Innov 2021;6:346–73. https://doi.org/10.1504/IJMRI.2021.116234.

[4] Iannuzzo A, Block P, Angelillo M, Gesualdo A. A continuous energy-based numerical approach to predict fracture mechanisms in masonry structures: CDF method. Comput Struct 2021;257:. https://doi.org/10.1016/j.compstruc.2021.106645106645.

[5] Iannuzzo A, Van Mele T, Block P. Piecewise rigid displacement (PRD) method: a limit analysis-based approach to detect mechanisms and internal forces through two dual energy criteria. Mech Res Commun 2020;107:. https://doi.org/10.1016/j.mechrescom.2020.103557103557.

[6] Makris N, Alexakis H. The effect of stereotomy on the shape of the thrust-line and the minimum thickness of semicircular masonry arches. Arch Appl Mech 2013;83:1511–33. https://doi.org/10.1007/s00419-013-0763-4.

[7] Chiozzi A, Grillanda N, Milani G, Tralli A. UB-ALMANAC: An adaptive limit analysis NURBS-based program for the automatic assessment of partial failure mechanisms in masonry churches. Eng Fail Anal 2018;85:201–20. https://doi.org/10.1016/j.engfailanal.2017.11.013.

[8] Chiozzi A, Malagù M, Tralli A, Cazzani A. ArchNURBS: NURBS-Based Tool for the Structural Safety Assessment of Masonry Arches in MATLAB. J Comput Civ Eng 2016;30:4015010. https://doi.org/10.1061/(asce)cp.1943-5487.0000481.

[9] Grillanda N, Valente M, Milani G. ANUB-Aggregates: a fully automatic NURBS-based software for advanced local failure analyses of historical masonry aggregates. Bull Earthq Eng 2020;18:3935–61. https://doi.org/10.1007/s10518-020-00848-6.

[10] Portioli F. Rigid block modelling of historic masonry structures using mathematical programming: a unified formulation for non-linear time history, static pushover and limit equilibrium analysis. Bull Earthq Eng 2020;18:211–39. https://doi.org/10.1007/s10518-019-00722-0.

[11] Livesley RK. Limit Analysis of Structures Formed from Rigid Blocks. Int J Numer Methods Eng 1978;12:1853–71.

[12] Livesley RK. A computational model for the limit analysis of three-dimensional masonry structures. Meccanica 1992;27:161–72. https://doi.org/10.1007/BF00430042.

[13] Drucker DC. Coulomb Friction, Plasticity, and Limit Loads. J Appl Mech 1954;21:71–4. https://doi.org/10.1115/1.4010821.

[14] Michalowski R, Mroz Z. Associated and non-associated sliding rules in contact friction problems. Arch Mech Stosow 1978:259–76.

[15] Portioli F, Casapulla C, Gilbert M, Cascini L. Limit analysis of 3D masonry block structures with non-associative frictional joints using cone programming. Comput Struct 2014;143:108–21. https://doi.org/10.1016/j.compstruc.2014.07.010.

[16] Ferris MC, Tin-Loi F. Limit analysis of frictional block assemblies as a mathematical program with complementarity constraints. Int J Mech Sci 2001;43:209–24. https://doi.org/10.1016/S0020-7403(99)00111-3.

[17] Gilbert M, Casapulla C, Ahmed HM. Limit analysis of masonry block structures with non-associative frictional joints using linear programming. Comput Struct 2006;84:873–87. https://doi.org/10.1016/j.compstruc.2006.02.005.

[18] Orduña A, Lourenço PB. Three-dimensional limit analysis of rigid blocks assemblages. Part II: Load-path following solution procedure and validation. Int J Solids Struct 2005;42:5161–80. https://doi.org/10.1016/j.ijsolstr.2005.02.011.

[19] Chiozzi A, Milani G, Tralli A. Fast Kinematic Limit Analysis of FRP-Reinforced Masonry Vaults. II: Numerical Simulations. J Eng Mech 2017;143:04017072. https://doi.org/10.1061/(asce)em.1943-7889.0001268.

[20] Milani G, Valente M, Fagone M, Rotunno T, Alessandri C. Advanced non-linear numerical modeling of masonry groin vaults of major historical importance: St John Hospital case study in Jerusalem. Eng Struct 2019;194:458–76. https://doi.org/10.1016/j.engstruct.2019.05.021.

[21] Ascione L, Feo L, Fraternali F. Load carrying capacity of 2D FRP/strengthened masonry structures. Compos Part B Eng 2005;36:619–26. https://doi.org/10.1016/j.compositesb.2004.12.004.

[22] Milani G, Milani E, Tralli A. Upper bound limit analysis model for FRP-reinforced masonry curved structures. Part II: Structural analyses Comput Struct 2009;87:1534–58. https://doi.org/10.1016/j.compstruc.2009.07.010.

[23] Drosopoulos GA, Stavroulakis GE, Massalas CV. FRP reinforcement of stone arch bridges: Unilateral contact models and limit analysis. Compos Part B Eng 2007;38:144–51. https://doi.org/10.1016/j.compositesb.2006.08.004.

[24] Caporale A, Feo L, Hui D, Luciano R. Debonding of FRP in multi-span masonry arch structures via limit analysis. Compos Struct 2014;108:856–65. https://doi.org/10.1016/j.compstruct.2013.10.006.

[25] Caporale A, Feo L, Luciano R, Penna R. Numerical collapse load of multi-span masonry arch structures with FRP reinforcement. Compos Part B Eng 2013;54:71–84. https://doi.org/10.1016/j.compositesb.2013.04.042.

[26] Caporale A, Luciano R, Rosati L. Limit analysis of masonry arches with externally bonded FRP reinforcements. Comput Methods Appl Mech Eng 2006;196:247–60. https://doi.org/10.1016/j.cma.2006.03.003.

[27] Milani G, Milani E, Tralli A. Upper Bound limit analysis model for FRP-reinforced masonry curved structures. Part I: Unreinforced masonry failure surfaces. Comput Struct 2009;87:1516–33. https://doi.org/10.1016/j.compstruc.2009.07.007.

[28] Anania L, D'Agata G. Limit analysis of vaulted structures strengthened by an innovative technology in applying CFRP. Constr Build Mater 2017;145:336–46. https://doi.org/10.1016/j.conbuildmat.2017.03.212.

[29] Nodargi NA, Intrigila C, Bisegna P. A variational-based fixed-point algorithm for the limit analysis of dry-masonry block structures with non-associative Coulomb friction. Int J Mech Sci 2019;161–162:. https://doi.org/10.1016/j.ijmecsci.2019.105078105078.

[30] CNR-DT200. Guide for the design and construction of externally bonded FRP systems for strengthening existing structures. CNR, National Research Council, Italy, n.d.

[31] Panizza M, Garbin E, Valluzzi MR. Peel strength testing of FRP applied to clay bricks. In: Proc 8th Int Conf Fract Mech Concr Concr Struct, IA-FraMCoS. Spain: Ciudad Real; 2013. p. 562–70.
[32] Carozzi FG, Poggi C, Bertolesi E, Milani G. Ancient masonry arches and vaults strengthened with TRM, SRG and FRP composites: Experimental evaluation. Compos Struct 2018;187:466–80. https://doi.org/10.1016/j.compstruct.2017.12.075.
[33] Bertolesi E, Milani G, Carozzi FG, Poggi C. Ancient masonry arches and vaults strengthened with TRM, SRG and FRP composites: Numerical analyses. Compos Struct 2018;187:385–402. https://doi.org/10.1016/j.compstruct.2017.12.021.
[34] Girardello P, Pappas A, da Porto F, Valluzzi RM. Experimental testing and numerical modelling of masonry vaults. In: Int Conf Rehabil Restor Struct. India: Chennai; 2013. p. 1–10.
[35] De Santis S, de Felice G. Steel reinforced grout systems for the strengthening of masonry structures. Compos Struct 2015;134:533–48. https://doi.org/10.1016/j.compstruct.2015.08.094.
[36] Bilotta A, Lignola GP. Effect of fiber-to-matrix bond on the performance of inorganic matrix composites. Compos Struct 2021;265:. https://doi.org/10.1016/j.compstruct.2021.113655113655.
[37] Jing L, Yin S, Aslani F, Liu S. Statistical analysis of the bonding properties of the fabric-reinforced cementitious matrix for strengthening masonry structures. Adv Struct Eng 2021;24:3057–69. https://doi.org/10.1177/13694332211017994.
[38] Al-Lami K, Calabrese AS, Colombi P, D'antino T. Effect of wet-dry cycles on the bond behavior of fiber-reinforced inorganic-matrix systems bonded to masonry substrates. Materials (Basel) 2021;14(20):6171. https://doi.org/10.3390/ma14206171.
[39] Wang X, Lam CC, Iu VP. Bond behaviour of steel-TRM composites for strengthening masonry elements: experimental testing and numerical modelling. Constr Build Mater 2020;253:. https://doi.org/10.1016/j.conbuildmat.2020.119157119157.
[40] Rotunno T, Fagone M, Bertolesi E, Grande E, Milani G. Single lap shear tests of masonry curved pillars externally strengthened by CFRP strips. Compos Struct 2018;200:434–48. https://doi.org/10.1016/j.compstruct.2018.05.097.
[41] Fishwick RJ. Limit Analysis of Rigid Block Structures, Department of Civil Engineering, University of Portsmouth; 1996. Ph.D. thesis. https://doi.org/10.1007/978-1-349-95810-8_1241.